AGU PUBLICATIONS

JGR

Journal of Geophysical Research: Oceans

RESEARCH ARTICLE

10.1002/2017JC013411

Key Points:
- Horizontal and vertical advection, production, and dissipation are the dominant terms in the near-bed TKE balance
- A two-dimensional (horizontal + vertical) clockwise circulation advects wave breaking TKE through the near-bed layer
- Flow nonuniformity and the presence of energetic anisotropic wave breaking turbulence enhances near-bed turbulence production

Correspondence to:
J. van der Zanden,
j.vanderzanden@utwente.nl

Citation:
van der Zanden, J., van der A, D. A., Cáceres, I., Hurther, D., McLelland, S. J., Ribberink, J. S., & O'Donoghue, T. (2018). Near-bed turbulent kinetic energy budget under a large-scale plunging breaking wave over a fixed bar. *Journal of Geophysical Research: Oceans*, *123*, 1429–1456. https://doi.org/10.1002/2017JC013411

Received 31 AUG 2017
Accepted 28 JAN 2018
Accepted article online 5 FEB 2018
Published online 24 FEB 2018

Near-Bed Turbulent Kinetic Energy Budget Under a Large-Scale Plunging Breaking Wave Over a Fixed Bar

Joep van der Zanden[1,2], Dominic A. van der A[1], Iván Cáceres[3], David Hurther[4], Stuart J. McLelland[5], Jan S. Ribberink[2], and Tom O'Donoghue[1]

[1]School of Engineering, University of Aberdeen, Aberdeen, UK, [2]Department of Water Engineering and Management, University of Twente, Enschede, the Netherlands, [3]Laboratori d'Enginyeria Marítima, Universitat Politècnica de Catalunya, Barcelona, Spain, [4]LEGI, CNRS, University of Grenoble Alpes, Grenoble, France, [5]Department of Geography, Environment and Earth Sciences, University of Hull, Cottingham Road, Hull, UK

Abstract Hydrodynamics under regular plunging breaking waves over a fixed breaker bar were studied in a large-scale wave flume. A previous paper reported on the outer flow hydrodynamics; the present paper focuses on the turbulence dynamics near the bed (up to 0.10 m from the bed). Velocities were measured with high spatial and temporal resolution using a two component laser Doppler anemometer. The results show that even at close distance from the bed (1 mm), the turbulent kinetic energy (TKE) increases by a factor five between the shoaling, and breaking regions because of invasion of wave breaking turbulence. The sign and phase behavior of the time-dependent Reynolds shear stresses at elevations up to approximately 0.02 m from the bed (roughly twice the elevation of the boundary layer overshoot) are mainly controlled by local bed-shear-generated turbulence, but at higher elevations Reynolds stresses are controlled by wave breaking turbulence. The measurements are subsequently analyzed to investigate the TKE budget at wave-averaged and intrawave time scales. Horizontal and vertical turbulence advection, production, and dissipation are the major terms. A two-dimensional wave-averaged circulation drives advection of wave breaking turbulence through the near-bed layer, resulting in a net downward influx in the bar trough region, followed by seaward advection along the bar's shoreward slope, and an upward outflux above the bar crest. The strongly nonuniform flow across the bar combined with the presence of anisotropic turbulence enhances turbulent production rates near the bed.

Plain Language Summary The flow of water under wind-driven waves near the coast is highly energetic, leading to the production of chaotic, "turbulent" fluid motions. Turbulence plays an important role in the flow and the transport of sediment under waves. Therefore, understanding turbulence dynamics is crucial to understanding the behavior of waves and their effects on shoreline processes (e.g., beach erosion). Previous research shows that the breaking of waves leads to a massive production of turbulent energy, but the vertical and horizontal spreading of turbulence is not properly understood. Through experiments in a large-scale wave flume, using acoustic and laser-based measurement instrumentation, the behavior of turbulent energy under breaking waves is systematically investigated. Results show that wave breaking alters turbulence dynamics over the full water column, from the water surface all the way down to the bed. Turbulence is spread horizontally and vertically by "undertow" currents generated by the breaking wave. Moreover, wave breaking turbulence leads to the production of additional turbulence in the water column. The new insights in this paper can be used to further develop computational models for the flow and transport of sediment under breaking waves.

1. Introduction

The wave bottom boundary layer (WBL) is defined as the lowest part of the water column where orbital velocities are significantly affected by the presence of the bed (Nielsen, 1992). The WBL is important in terms of bed shear stress, sediment transport, and the production of turbulent vortices through velocity shear. Turbulence contributes to momentum exchange and particle suspension, and should therefore be included in near-shore hydrodynamic and morphodynamic numerical models.

Much of our knowledge of WBL turbulence dynamics originates from flow visualizations (Carstensen et al., 2010, 2012; Hayashi & Ohashi, 1982; Sarpkaya, 1993) and turbulent velocity measurements (Akhavan et al., 1991; Hino et al., 1983; Jensen et al., 1989; Sleath, 1987; van der A et al., 2011; Yuan & Dash, 2017) in oscillatory flow tunnel studies. Turbulence measurements in the WBL under nonbreaking surface waves are limited, but have been conducted at full scale (Conley & Inman, 1992; Foster et al., 2006) and small-scale (Henriquez et al., 2014; Kemp & Simons, 1982, 1983), generally showing behavior that is similar to tunnel observations. Direct numerical simulations (e.g., Costamagna et al., 2003; Pedocchi et al., 2011; Scandura, 2013; Scandura et al., 2016; Vittori & Verzicco, 1998) have further advanced the understanding of oscillatory boundary layer turbulence. In wave-generated bed boundary layers at full scale, turbulence is unsteady and builds up and decays during each half-cycle. Turbulence is initially generated at the bed during the accelerating flow phase in the form of longitudinal low-speed streaks, which then break up into smaller-scale vortices that merge and produce a burst of turbulence during the decelerating stage of the half-cycle (Carstensen et al., 2010; Costamagna et al., 2003; Hayashi & Ohashi, 1982; Scandura et al., 2016; Vittori & Verzicco, 1998). Consequently, turbulent intensities and Reynolds stress at the bed increase during flow acceleration and reach a maximum during the decelerating phase (e.g., Jensen et al., 1989). As turbulence diffuses upward, turbulent intensities and Reynolds stresses show a progressive time lag with elevation, relative to their phase behavior at the bed (e.g., Hayashi & Ohashi, 1982; Hino et al., 1983; Jensen et al., 1989; van der A et al., 2011). The precise spatial and temporal turbulent behavior of oscillatory flows depends on Reynolds number and bed roughness (e.g., Jensen et al., 1989).

Under breaking waves, the dynamics of turbulence inside the WBL are altered. A breaking wave forms large-scale coherent vortices, which have been well documented on the basis of small-scale wave flume observations (Chiapponi et al., 2017; Kimmoun & Branger, 2007; LeClaire & Ting, 2017; Longo, 2009; Nadaoka et al., 1989; Peregrine, 1983; Stansby & Feng, 2005). These wave breaking vortices can invade the WBL and reach the bed, as shown in wave flumes at small (Cox & Kobayashi, 2000; Nadaoka et al., 1989; Sumer et al., 2013) and large (van der Zanden et al., 2016) scales. For these conditions, local bed-generated turbulence is not the only source of near-bed TKE: horizontal and vertical advection and diffusion of external turbulence cannot be neglected. In addition, these vortices may alter the turbulent production process and production rate in the WBL. Turbulent production is explained by turbulent vortices entraining nonturbulent fluid, which then break up to random turbulence fluctuations due to internal shear (Hussain, 1986; Pope, 2000). This mechanism of TKE production depends on the strength and orientation of the ambient turbulent structures, and is different for a situation with interacting bed-generated and breaking-generated vortices compared to a purely oscillatory WBL.

The incursion of breaking-generated turbulence into the WBL has significant effects on near-bed hydrodynamics and sand transport. External turbulence enhances the momentum exchange between the free-stream and WBL, hence altering the flow inside the WBL (Fredsøe et al., 2003). Breaking-generated turbulence enhances magnitudes of instantaneous bed shear stresses (Cox & Kobayashi, 2000; Deigaard et al., 1991) and suspended sediment pick-up and transport rates (Nadaoka et al., 1988; van der Zanden et al., 2017a; Zhou et al., 2017). Consequently, numerical simulations of velocities, suspended sediment concentrations, and ultimately net sand transport rates and morphology in the surf zone, require accurate predictions of TKE, especially near the bed, where the majority of sediment transport occurs (van der Zanden et al., 2017a). However, existing turbulence closure models tend to systematically overestimate TKE levels under breaking waves, both above (Brown et al., 2016; Christensen, 2006; Lin & Liu, 1998) and inside (Fernandez-Mora et al., 2016) the WBL.

In a recent laboratory experiment involving a barred sand bed profile, van der Zanden et al. (2016) studied for the first time the WBL flow and near-bed TKE under a large-scale plunging wave. Their measurements showed that wave breaking turbulence invades the WBL in the breaking region, leading to a significant increase in near-bed TKE compared to the shoaling zone, hence reaffirming the aforementioned observations from small-scale wave flumes. However, due to instrumental limitations, their experiment did not enable an in-depth analysis of the physical mechanisms behind the spatiotemporal variation of near-bed TKE, such as the importance of locally versus externally produced turbulence. Therefore, the objective of the present study is to gain more insight into the physical processes that drive the near-bed spatiotemporal behavior of turbulence under plunging waves. This will be achieved by systematically investigating the dominant terms in the TKE budget, hence following an approach similar to previous studies on outer-flow

turbulence under small-scale breaking waves (Chang & Liu, 1999; Clavero et al., 2016; Melville et al., 2002; Ting & Kirby, 1995). Because the present study focuses on the concurrent effects of breaking-generated and bed-shear-generated turbulence on near-bed TKE, it is important that the WBL flow is in a turbulent flow regime that is representative for prototype waves at natural beaches. For this reason, the experiments are conducted at large-scale.

The paper is organized as follows. Section 2 describes the experiments, data treatment, and the methodology used to quantify the TKE budget terms. Section 3 presents results for the phase-averaged and time-averaged velocities at outer-flow ($z - z_{bed} > 0.1$ m) and near-bed ($z - z_{bed} < 0.1$ m) elevations. Section 4 presents the primary turbulence statistics and a systematic investigation of the near-bed TKE budget terms. The discussion (section 5) addresses the uncertainties in the results and the implications of the results for turbulence modeling in the surf zone. Section 6 summarizes the main conclusions.

2. Methodology

2.1. Experimental Facility and Bed Profile

The experiment was conducted in the 100 m long, 3 m wide, and 4.5 m deep CIEM wave flume at the Polytechnic University of Catalunya in Barcelona. The flume is equipped with a wedge-type wave paddle and steering signals are generated based on first-order wave generation. Measurements for the present study were collected during the same experimental campaign as that reported by van der A et al. (2017), who focused on the outer-flow hydrodynamics.

Figure 1 shows the fixed bed profile in the wave flume as measured with echo sounders from a mobile carriage. The profile consists of an 18 m long, 1:12 offshore slope, a 0.6 m high breaker bar (measured from crest to trough), followed by a 10 m long, 1:125 slope and a 1:7 sloping beach. The profile was generated during a preceding mobile-bed experiment (van der Zanden et al., 2016) by running the same regular wave condition as for the present study for 3 h over a medium-sand bed profile that initially consisted of a 1:10 offshore slope and an 18 m long, 1.35 m high horizontal test section. The sand bed profile was homogenized by flattening out bedforms and by removing any lateral (cross-flume) asymmetry, and was then fixed by laying a 0.2 m thick layer of concrete over the profile; the concrete was homogenized in lateral direction and allowed to cure for about 40 days prior to the start of the experiment.

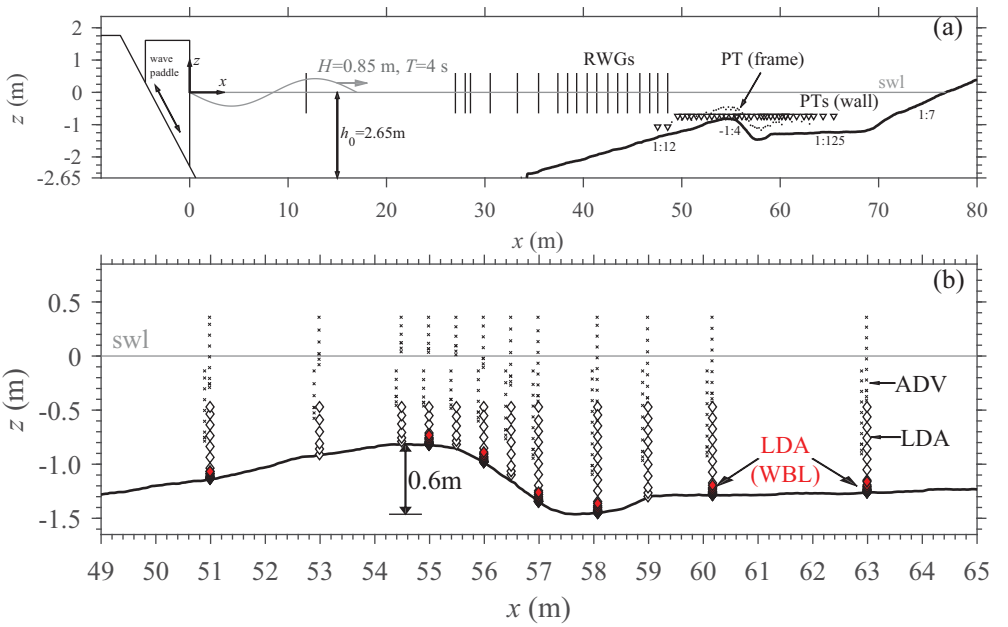

Figure 1. Experimental setup. (a) Locations of water surface elevation measurements by resistive wave gauges (RWGs; vertical black lines), side-wall-deployed pressure transducers (PTs wall; triangles), and mobile-frame PT (dots). (b) Close-up of barred test section, indicating velocity measurement locations by ADV (crosses), and LDA (diamonds). Red diamonds mark detailed near-bed measurements with LDA at seven cross-shore locations.

Table 1
Wave and Velocity Statistics at Free-Stream Elevation ($\zeta \approx 0.10$ m) at Seven WBL Measurement Locations

x (m)	h (m)	H (m)	dz_{bed}/dx	$\bar{u}$ (m/s)	$\tilde{u}_{rms}$ (m/s)	$\langle u \rangle_{max}$ (m/s)	$\langle u \rangle_{min}$ (m/s)	a (m)	k_s (mm)	a/k_s	Re
51.0	1.10	0.77	0.10	−0.13	0.54	1.01	−0.70	0.46	1	460	5.2×10^5
55.0	0.78	0.48	−0.02	−0.23	0.51	0.73	−0.96	0.43	1	430	4.1×10^5
56.0	0.94	0.36	−0.26	−0.67	0.29	−0.06	−1.06	0.25	3	80	1.6×10^5
57.0	1.34	0.43	−0.33	−0.28	0.23	0.23	−0.47	0.20	3	70	1.0×10^5
58.1	1.45	0.42	−0.02	−0.16	0.19	0.23	−0.34	0.16	1	160	6.2×10^4
60.2	1.30	0.39	0.01	−0.22	0.22	0.22	−0.49	0.19	1	190	8.5×10^4
63.0	1.26	0.38	0.07	−0.18	0.27	0.34	−0.49	0.23	1	230	1.2×10^5

The surface roughness, k_s, was quantified using boundary layer velocity measurements from the wave shoaling region by applying the log-law fitting procedure of Dixen et al. (2008) to velocity profiles measured at the phase of maximum onshore velocity: first, the straight-line fraction of $u(\zeta)$ versus $^{10}\log(\zeta)$ was identified; second, the vertical displacement $\Delta\zeta$ was found by vertically shifting the data until the number of velocity measurements satisfying a linear trend was maximum; finally, the best linear fit was calculated (coefficient of determination $r^2 > 0.99$). This method yielded a roughness $k_s = 1.4$ ($\pm$ 1) mm, where the uncertainty was estimated by varying $\Delta\zeta$ by $\pm$ 1 mm (corresponding to the vertical spacing of measurements close to the bed). The roughness was reasonably uniform across the profile, except on the lee-side slope of the bar, where coarser aggregates were more exposed as cement leaked from the slope during the curing process. Unfortunately, the measurements did not allow quantification of k_s at this region, but we estimate a bed roughness that is twice higher than at the shoaling and inner surf zones, i.e., $k_s = 3$ ($\pm$ 2) mm. Based on the local Reynolds number $Re = a \cdot \langle \tilde{u} \rangle_{max}/\nu$ (where a is the orbital semi-excursion amplitude and $\nu = 1.0 \cdot 10^{-6}$ m^2/s is the kinematic viscosity) and bed roughness estimates (see values in Table 1), the WBL flow is in the rough turbulent regime at locations seaward of the bar and in the transitional regime shoreward of the bar (following definitions by Jonsson, 1980).Throughout the paper, the coordinate system has its x-origin at the toe of the wave paddle and is defined positively toward the beach; the lateral y-coordinate has its origin at the right-hand side-wall of the flume when facing the beach and is positive toward the flume's centerline; the vertical coordinate z is defined positively upward, with $z = 0$ at the still water level. Annotation ζ is used to express elevations with respect to the local bed level z_{bed} (i.e., $\zeta = z - z_{bed}$). Velocity components in x, y, and z direction are denoted u, v, and w, respectively.

2.2. Test Condition

The water depth, h, in the deeper part of the wave flume was 2.65 m. Regular waves were generated based on first-order wave theory, with wave period $T = 4$ s and a measured wave height $H_p = 0.76$ m near the wave paddle ($x = 11.8$ m). The deep-water surf similarity parameter $\xi_0 = \tan\beta/\sqrt{H_0/L_0} = 0.46$, where $\tan\beta$ is the 1:12 beach slope, H_0 is the deep-water wave height that corresponds to H_p following linear wave theory, and $L_0 = gT^2/2\pi$ is the deep-water wave length. Breaking waves were of the plunging type, which is consistent with $\xi_0 = 0.46$, following the classification of Smith and Kraus (1991) for barred beaches.

The breaking process is described in detail by van der A et al. (2017) and was classified following the terminology of Smith and Kraus (1991). The bar crest is at $x = 54.5$ m. The wave starts to overturn at $x = 52$ m ("break point"), hits the water surface above the bar crest at $x = 54.5$ m ("plunge point"), and pushes up a wedge of water that develops into a surf bore at $x = 58.5$ m ("splash point"). We follow Svendsen et al. (1978) by defining the (outer) breaking region as the region between the break point and the splash point; the regions seaward and shoreward from the the breaking region are termed shoaling zone and inner surf zone, respectively.

2.3. Measurements

Water surface elevations were measured at data rate $f_s = 40$ Hz using sidewall-mounted resistive wave gauges at 19 locations along the deeper part of the wave flume and along the shoaling zone (Figure 1a). In the breaking and inner surf zones, measurements of dynamic pressure were obtained at $f_s = 40$ Hz with pressure transducers deployed from the flume side-walls and from a mobile measuring frame. The pressure measurements were converted to water surface elevation using linear wave theory. More details on the water surface measurements are provided by van der A et al. (2017).

Velocities were measured at 12 cross-shore locations along the bar using a two-component laser Doppler anemometer (LDA) and two acoustic Doppler velocimeters (ADV) deployed from a measurement frame attached to a carriage on top of the flume. The two-component backscatter LDA system (Dantec FiberFlow) consisted of a 14 mm diameter submersible transducer probe with 50 mm focal length powered by a 300 mW argon-ion air-cooled laser. The LDA measured the u and w velocity components in an ellipsoidal shaped measurement volume of 115 μm maximum diameter and 2 mm length in y direction. The data rate of the LDA depends on seeding particle density and velocity magnitude and therefore varied throughout the wave cycle and per location. For the present experiment, f_s typically varied between 100 and 600 Hz. The three-component ADVs (Nortek Vectrino) measured velocities at outer-flow elevations with $f_s = 100$ Hz. The ADVs were orientated horizontally (side-looking). Their cylindrical shaped measurement volume was approximately 6 mm in diameter and 2.8 mm in the y direction. The vertical spacing between the LDA and the ADVs was 0.33 m (for the lower ADV) and 0.83 m (for the upper ADV). The lateral coordinate of the LDA measurement volume was $y = 1.9$ m, i.e., at 1.1 m from the nearest side-wall and at 0.4 m from the flume's centerline, which ensures minimum flow perturbation by the side-walls.

The "mobile frame" allowed the instruments to be positioned with 1 cm accuracy in the horizontal and submillimeter accuracy in the vertical. Vertical repositioning was done manually using a spindle and the elevation was recorded using a magnetic tape sensor. More details on the frame are provided by Ribberink et al. (2014). One run consisted of 38 min of wave generation. Video recordings showed that the breaking point gradually shifted during the first 400 s. After this, the breaking location stabilized, indicating that a hydrodynamic quasi-equilibrium was established. The term quasi-equilibrium is used because the cross-shore location of wave breaking maintained a slight and random variability ($\pm$ 0.2 m). Subsequently, three successive measurements were made for a duration of 10 min each (150 wave cycles), by positioning the frame at three elevations. Hence, during one run, 10 min velocity time series were recorded at nine elevations (three instruments x three frame positions). A total of 78 runs were conducted with the frame positioned at 12 cross-shore locations and at different vertical elevations, resulting in vertical profiles of velocity that cover the WBL up to wave crest level with high vertical resolution ($\Delta z \leq 0.10$ m) as shown in Figure 1b.

Additional detailed WBL LDA velocity measurements were made at seven cross-shore locations ($x = 51.0$, 55.0, 56.0, 57.0, 58.1, 60.2, and 63.0 m), at 14 elevations ($\zeta = 1$, 2, 3, 4, 5, 7, 10, 14, 19, 26, 36, 51, 70, and 94 mm) (Figure 1b). To facilitate these near-bed measurements the LDA was orientated at an angle of 8.9° to the horizontal and the bed level was found by slowly lowering the frame until the LDA's focal point intersected the top of the bed, the intersection point being determined by a sharp increase in the backscattered light intensity. The vertical positioning has an estimated accuracy of $\pm$ 0.5 mm.

Data acquisition was started on a 40 Hz analogue trigger pulse, corresponding to a $1/40 = 0.025$ s accuracy in timing between different LDA acquisitions. To improve this accuracy, the lowest ADV measurement (always at free-stream elevation) was recorded by the LDA internal acquisition system at the same f_s as the LDA. By matching the free-stream velocities measured by ADV for all acquisitions, the synchronization between different LDA measurements was improved to an accuracy of $\pm$0.01 s.

2.4. Data Processing

The standing wave which occurred in the flume, with frequency $f = 0.022$ Hz and amplitude of O(cm), was removed from the water surface and velocity time series through a high-pass filter with a cutoff frequency of 0.125 Hz ($= 0.5/T$). ADV data were cleaned using a combination of signal-to-noise ratio and correlation threshold criteria and outlier identification, as described by van der A et al. (2017). The LDA data scarcely suffered from spurious measurements because measurements were SNR-validated during acquisition and no data were recorded when air bubbles blocked the path of the laser beams. Any remaining outliers were identified as instantaneous velocity measurements that deviated from more than five times the standard deviation from the ensemble-median at a given wave phase. These data points, which form less than 0.1% of the total number of LDA measurements, were removed from the record, and not replaced.

Phase-averaged velocities are indicated by angular brackets and were calculated following a conditional averaging method (e.g., Petti & Longo, 2001):

$$\langle u(t)\rangle = \frac{1}{N}\sum_{n=0}^{N-1} u(t+t_n) \;\; 0 \le t < T\,. \tag{1}$$

Here, N is the number of wave cycles and t_n is the cyclic trigger, defined as the time instant of the nth zero-up crossing of the water surface measured by the resistive wave gauge at $x = 48.6$ m (shoaling region). Water surface elevations were phase-averaged over 30 min (450 waves) and over different runs. Velocity measurements were phase-averaged over the 10 min measurement duration (150 waves) at each measurement elevation. For the irregularly sampled LDA measurements, the data were averaged, accounting for seeding particle residence time, over intervals of 1/128 s centered on each phase instant. All phase-averaged results were time-referenced such that $t/T = 0$ corresponds to the zero-up crossing of the water surface at $x = 50$ m.

Wave-averaged velocities are indicated by an overbar:

$$\overline{u} = \frac{1}{T}\int_0^T \langle u\rangle \mathrm{d}t\,. \tag{2}$$

The phase-averaged velocity $\langle u\rangle = \bar{u} + \tilde{u}$, with $\tilde{u}$ being the periodic velocity. The turbulent velocity u' is defined as the difference between the instantaneous velocity u and the phase-averaged velocity $\langle u\rangle$. The same methodology is applied to decompose the vertical velocity w. Note that following this definition of u', any phase-coherent velocity contributions of the plunging jet are considered part of the periodic velocity $\tilde{u}$ and do not contribute to the computed TKE (as also pointed out by e.g., Nadaoka et al., 1989). Furthermore, following this decomposition, any deviations of u from $\langle u\rangle$ emerging from small variations in wave generation, wave celerity and breaking location, potentially lead to wave bias in the turbulence signal (also termed "pseudo-turbulence") (e.g., Nadaoka et al., 1989; Scott et al., 2005; Svendsen, 1987). Such wave bias appears in the spectra of u' and w' as peaks at the frequencies of the primary wave and its higher harmonics, and in the integrated cospectrum (ogive) of $u'w'$ (Feddersen & Williams, 2007) as stepwise increments at these frequencies. Therefore, the spectra and ogives were examined for all measurements, yet no such wave bias was evident. For this reason, we expect minor contributions ($< 5\%$) of pseudo-turbulence to u'_{rms} and w'_{rms}.

It is expected that velocity streamlines close to the bed follow the local bed inclination. In order to facilitate comparison with oscillatory boundary layer observations in tunnels and under nonbreaking waves, velocities were transformed to a bed-parallel (u_{R}) and bed-normal (w_{R}) component:

$$\begin{aligned} u_{\mathrm{R}} &= u\cdot\cos\beta + w\cdot\sin\beta,\\ w_{\mathrm{R}} &= w\cdot\cos\beta - u\cdot\sin\beta\,, \end{aligned} \tag{3}$$

with $\beta = \mathrm{atan}(\mathrm{d}z_{\mathrm{bed}}/\mathrm{d}x)$ the local bed slope, which was found by rotating velocities such that the root-mean-square $\tilde{w}_{\mathrm{R}}$ at $\zeta = 0.01$ m is minimized. Values of β estimated in this way were within 0.05° agreement with $\mathrm{atan}(\mathrm{d}z_{\mathrm{bed}}/\mathrm{d}x)$ obtained from the measured bed profile.

To reduce uncertainty in the estimated TKE budget terms, the analysis which follows considers depth-averaged turbulence within a near-bed layer that is defined here as $\zeta = 0$ to 0.10 m, where the latter value corresponds roughly to the upper measure of the WBL thickness based on a 5% velocity defect (e.g., Sleath, 1987) at $x = 51.0$ m. The depth-averaged quantities are indicated by a hat symbol, i.e., for arbitrary variable ψ:

$$\widehat{\psi} = \frac{1}{D - z_{\mathrm{b}}}\int_{z_{\mathrm{b}}}^{D} \psi \mathrm{d}\zeta\,, \tag{4}$$

where $z_{\mathrm{b}} = 0.001$ m and $D \approx 0.10$ m are the bottom and top levels of the near-bed control volume, respectively. The free-stream velocity u_∞ is defined at the top of the near-bed layer, i.e., at $\zeta = D$.

2.5. Turbulent Kinetic Energy Budget

For the two-component LDA, phase-averaged turbulent kinetic energy $\langle k\rangle$ (per unit mass) is calculated as

$$\langle k\rangle = 0.5 \cdot 1.47\left(\langle u'^2\rangle + \langle w'^2\rangle\right), \tag{5}$$

where the factor 1.47 was proposed by Svendsen (1987) for the outer region of the wave bottom boundary layer. The two-dimensional (x, z) budget equation for phase-averaged TKE reads (Pope, 2000; Tennekes & Lumley, 1972):

$$\frac{\partial\langle k\rangle}{\partial t} = \overbrace{-\left(\frac{\partial\langle u\rangle\langle k\rangle}{\partial x} + \frac{\partial\langle w\rangle\langle k\rangle}{\partial z}\right)}^{\text{advection},\,\mathcal{A}} \overbrace{-\left(\frac{\partial\langle u'k'\rangle}{\partial x} + \frac{\partial\langle w'k'\rangle}{\partial z}\right)}^{\text{turbulent diffusion},\,\mathcal{D}} \overbrace{-\frac{1}{\rho}\left(\frac{\partial\langle u'p'\rangle}{\partial x} + \frac{\partial\langle w'p'\rangle}{\partial z}\right)}^{\text{pressure diffusion}}$$
$$\overbrace{-\nu\left(\frac{\partial^2\langle k\rangle}{\partial x^2} + \frac{\partial^2\langle k\rangle}{\partial z^2}\right)}^{\text{viscous diffusion}} + \overbrace{\mathcal{P}}^{\text{production}} - \overbrace{\varepsilon}^{\text{dissipation}}. \tag{6}$$

The six terms on the right-hand side of equation (6) denote, respectively, rates of horizontal and vertical advection ($\mathcal{A}$); turbulent diffusion ($\mathcal{D}$); pressure diffusion with p' being the instantaneous pressure fluctuation; viscous diffusion with ν being the kinematic viscosity; turbulence production ($\mathcal{P}$); and turbulence dissipation (ε). Depth-averaged over the near-bed layer and in the transformed coordinate system, the advective influx of TKE into the near-bed layer can be rewritten to

$$\widehat{\mathcal{A}} = -\frac{\mathrm{d}\widehat{\langle u_R\rangle}\,\widehat{\langle k\rangle}}{\mathrm{d}x} + \frac{\langle w_R(z_b)\rangle\langle k(z_b)\rangle}{D-z_b} - \frac{\langle w_R(D)\rangle\langle k(D)\rangle}{D-z_b} = \widehat{\mathcal{A}}_x + \mathcal{A}_z(z_b) + \mathcal{A}_z(D), \tag{7}$$

where the three terms on the right-hand side of equation (7) denote the near-bed, depth-averaged influx due to cross-shore advection along the bed ($\widehat{\mathcal{A}}_x$), the advective influx in the bed-normal direction from below ($\mathcal{A}_z(z_b)$), and the advective influx in the bed-normal direction at the top ($\mathcal{A}_z(D)$), respectively. Note that all terms are defined positively into the control volume, i.e., $\mathcal{A} > 0$ corresponds to an increase in near-bed TKE.

Similarly, the depth-averaged diffusion term is rewritten to

$$\widehat{\mathcal{D}} = -\frac{\mathrm{d}\widehat{\langle u'_R k'\rangle}}{\mathrm{d}x} + \frac{\langle w'_R k'\rangle(z_b)}{D-z_b} - \frac{\langle w'_R k'\rangle(D)}{D-z_b} = \widehat{\mathcal{D}}_x + \mathcal{D}_z(z_b) + \mathcal{D}_z(D). \tag{8}$$

In equations (7) and (8), the bed-normal influx at $\zeta = z_b$ (terms $\mathcal{A}_z(z_b)$ and $\mathcal{D}(z_b)$) can be evaluated only at the seven cross-shore locations for which we have detailed WBL velocity measurements (Figure 1b). The other two terms are evaluated at all 12 cross-shore measurement locations. This means that for five of the cross-shore locations, the cross-shore influx terms ($\widehat{\mathcal{A}}_x$ and $\widehat{\mathcal{D}}_x$) are based on measurements at only three elevations, which results in a random error in $\widehat{\mathcal{A}}_x$ and $\widehat{\mathcal{D}}_x$ of about 10%, estimated by intercomparing the two methods (3 versus 14 data points) at the other cross-shore locations. The $\widehat{\mathcal{A}}_x$ and $\widehat{\mathcal{D}}_x$ terms were calculated through a central-difference scheme using measurements at two adjacent locations and using the bed-parallel separation distance for Δx. The uncertainty in $\widehat{\mathcal{A}}_x$ due to the limited horizontal resolution was estimated to be in the range of 0 to 20%. This uncertainty was quantified by cubic interpolation of $\widehat{\langle u_R\rangle}\,\widehat{\langle k\rangle}$ to a finer horizontal spacing, and $\widehat{\mathcal{A}}_x$ was then compared between the original and the interpolated calculations.

The pressure transport term (third term on the right side of equation (6)) cannot be quantified from the measurements. The viscous diffusion term (fourth term in equation (6)) is assumed neglibly small compared to diffusion by turbulent velocities (second term). This was confirmed for small-scale breaking waves (e.g., Clavero et al., 2016), while for the present large-scale experiment the dominance of turbulent diffusion over molecular diffusion is even greater.

The production term consists of four contributions:

$$\mathcal{P} = -\langle u'w'\rangle\left(\frac{\partial\langle u\rangle}{\partial z} + \frac{\partial\langle w\rangle}{\partial x}\right) - \left(\langle u'^2\rangle\frac{\partial\langle u\rangle}{\partial x} + \langle w'^2\rangle\frac{\partial\langle w\rangle}{\partial z}\right), \tag{9}$$

i.e., contributions by shear stresses $\mathcal{P}_s$ (first two terms) and by normal stresses $\mathcal{P}_n$ (latter two terms). By estimating velocity gradients in the horizontal and vertical directions, it was found that $\left|\frac{\partial\langle w\rangle}{\partial x}\right| \ll \left|\frac{\partial\langle u\rangle}{\partial z}\right|$.

Therefore, the vertical velocity contribution to $\mathcal{P}_s$ ($-\langle u'w'\rangle \frac{\partial\langle w\rangle}{\partial x}$) is neglected. Assuming 2-D flow ($\frac{\partial}{\partial y}=0$), mass continuity requires that $\frac{\partial\langle u\rangle}{\partial x}=-\frac{\partial\langle w\rangle}{\partial z}$ which allows the normal stress contributions to be rewritten in terms of vertical gradients only. With these considerations equation (9) can be rewritten to

$$\mathcal{P}=\mathcal{P}_s+\mathcal{P}_n \approx -\langle u'_R w'_R\rangle \frac{\partial\langle u_R\rangle}{\partial z}-\left[\langle w'^2_R\rangle-\langle u'^2_R\rangle\right]\frac{\partial\langle w_R\rangle}{\partial z}, \tag{10}$$

from which follows that $\mathcal{P}_n = 0$ when turbulence is isotropic ($\langle w'^2_R\rangle=\langle u'^2_R\rangle$) or when the flow is uniform ($\frac{\partial\langle w_R\rangle}{\partial z}=-\frac{\partial\langle u_R\rangle}{\partial x}=0$). Equation (10) is evaluated using a central-difference scheme at the seven cross-shore locations with detailed WBL measurements. Note that the vertical resolution for calculating the velocity gradients is rather small ($\Delta z = O(1\text{ mm})$). Consequently, slight differences between experimental runs may lead to large errors in the estimated velocity gradients. Therefore, data points that deviated, by sign, from the overal trend of $d\bar{u}/dz$ or $d\overline{w}/dz$ at each cross-shore location were removed (25 out of 104 samples) prior to evaluation of equation (10). The predominant effect of removing these runs is a reduction in scatter in $\mathcal{P}(\zeta)$; the effect on depth-averaged $\widehat{\mathcal{P}}$ is limited (<10%). The estimates of $\mathcal{P}$ are insensitive to the applied velocity transformation prior to evaluating equation (10), but the transformation does lead to a redistribution between the $\mathcal{P}_s$ and $\mathcal{P}_n$ terms.

Turbulent dissipation rates ε were calculated based on autospectra of LDA-measured u, using two methods proposed for surf zone conditions. The well-established method of Trowbridge and Elgar (2001) for calculating time-averaged $\overline{\varepsilon}$ has been applied to outer-flow velocities from the present experimental campaign (van der A et al., 2017) and, to surf zone velocities measured in the field (Feddersen et al., 2007; Raubenheimer et al., 2004) and in the laboratory (Yoon & Cox, 2010). However, the method does not provide time-varying dissipation rates. Therefore, we also adopted a method similar to that of George et al. (1994) to compute surf-zone ε at an intrawave time scale. Both methods are based on the relation between turbulent dissipation rate and the velocity spectrum at inertial subrange frequencies (e.g., Pope, 2000):

$$E_{uu}(\kappa_x)=\frac{18}{55}C_k\varepsilon(\kappa_x)^{2/3}\kappa_x^{-5/3}. \tag{11}$$

Here, $E_{uu}(\kappa_x)$ is the energy spectrum as function of wave number κ_x in x direction and is defined such that the one-dimensional integrated spectrum equals the spatial variance of u; $C_k = 1.5$ is the Kolmogorov constant. In the present study, $E_{uu}(\kappa_x)$ could not be estimated directly since only local point measurements of u were made. Therefore, the temporal power spectral density $P_{uu}(\omega)$ (where $\omega = 2\pi f$ is the radian frequency) of u was translated into a wave number spectrum following Taylor's (1938) frozen-turbulence hypothesis, which assumes that turbulent fluctuations u' relate to the advection of locally isotropic turbulence by the (phase-)mean flow U (with $U \gg u'$), yielding $\kappa_x=\omega/U$ and $E_{uu}(\kappa_x)=P_{uu}(\omega)U$. This allows equation (11) to be rewritten to:

$$\varepsilon(\omega)=\left[\frac{55}{18}C_k{}^{-1}U^{-\frac{2}{3}}\omega^{\frac{5}{3}}P_{uu}(\omega)\right]^{3/2}. \tag{12}$$

First, following George et al. (1994), equation (12) was applied at an intrawave time scale over short time intervals Δt ($= T/24 \approx 0.17$ s). In the present study, turbulence is advected in horizontal and vertical directions. The advection speed U was therefore equated to the magnitude of the resultant phase-averaged velocity vector, i.e., $U=\langle|\vec{u}\,(t)|\rangle$ with $\langle\vec{u}\,(t)\rangle=(\langle u(t)\rangle,\langle w(t)\rangle)$. To be consistent with Taylor (1938), this also required using the spectrum of the velocity time series transformed in the direction of $\langle\vec{u}\,(t)\rangle$. This approach differs from that of George et al. (1994) who assumed negligible vertical advection. Note that close to the bed, U approaches 0 during flow reversals, hence potentially leading to asymptotic behavior in $\langle\varepsilon\rangle$. Nevertheless, as will be shown in section 4.5, no such bias in $\langle\varepsilon\rangle$ around flow reversals was observed.

Second, we adopted the methodology of Trowbridge and Elgar (2001) to compute the time-averaged dissipation rate $\overline{\varepsilon}$ for a wave-plus-current situation:

$$\overline{\varepsilon}(\omega)=\left[\frac{55}{18}C_k{}^{-1}\overline{u}^{-\frac{2}{3}}\omega^{\frac{5}{3}}I\left(\frac{\tilde{u}_{rms}}{\overline{u}}\right)^{-1}P_{uu}(\omega)\right]^{3/2}, \tag{13}$$

with

$$I\left(\frac{\tilde{u}_{\mathrm{rms}}}{\overline{u}}\right)=\frac{1}{\sqrt{2\pi}}\left(\frac{\tilde{u}_{\mathrm{rms}}}{\overline{u}}\right)^{2/3}\int_{-\infty}^{\infty}\left[x^2+2\frac{\overline{u}}{\tilde{u}_{\mathrm{rms}}}x+\frac{\overline{u}^2}{\tilde{u}_{\mathrm{rms}}^2}\right]^{1/3}\exp\left(-\frac{x^2}{2}\right)dx\,, \tag{14}$$

and $\tilde{u}_{\mathrm{rms}}$ is the root-mean-square periodic velocity.

For both methods, the LDA-measured velocities were linearly interpolated to a regular time series in order to compute $P_{uu}(\omega)$. This was done for each individual wave for equation (13) and for each wave phase Δt for equation (12); the frequency of the regular time series was equal to the mean sampling rate over each wave or phase ($f_s = 100$ to 600 Hz, corresponding to $\omega = 600$ to 3,800 rad/s). The assumptions of isotropic turbulence and $u' \ll U$ are only justified for small-scale eddies occuring at high frequencies. Comparison of P_{uu} and P_{ww} close to the bed ($\zeta = 0.001$ m) showed that turbulence was approximately isotropic only for $\omega > 300$ rad/s, so P_{uu} estimates for $\omega < 300$ rad/s were discarded. Equations (12) and (13) were then evaluated to calculate $\varepsilon(\omega)$, which, consistent with e.g., Feddersen et al. (2007), was approximately constant over the frequencies $\omega > 300$ rad/s corresponding to the inertial subrange. Following Feddersen et al. (2007), the logarithmic mean of $\varepsilon(\omega)$ over ω was computed to obtain $\langle\varepsilon(t)\rangle$ (using equation (12)) and $\overline{\varepsilon}$ (using equation (13)).

3. Water Surface Elevation and Flow Velocities

3.1. Outer-Flow Hydrodynamics

Details of the outer flow hydrodynamics for the experiment have been presented by van der A et al. (2017); a short summary of the most pertinent results is given here to aid understanding of the near-bed hydrodynamics.

Figure 2a shows the time-averaged velocity field and the envelope of minimum, mean, and maximum phase-averaged water surface elevation. The plunging jet strikes the water surface at $x = 54.5$ m at $t/T \approx 0.35$ and pushes up a wedge of water that strikes the water surface at $x \approx 58.5$ m at $t/T \approx 0.65$. This wedge develops into a surf bore which leads the remainder of the original wave (van der A et al., 2017). Wave breaking leads to a 50% reduction in wave height between the break point ($x = 52.0$ m) and the splash point ($x = 58.5$ m). Between these locations, the mean water level (mwl) changes from a set-down (≈ -0.025 m) to a setup ($\approx +0.025$ m). The first-order wave generation led to the presence of spurious

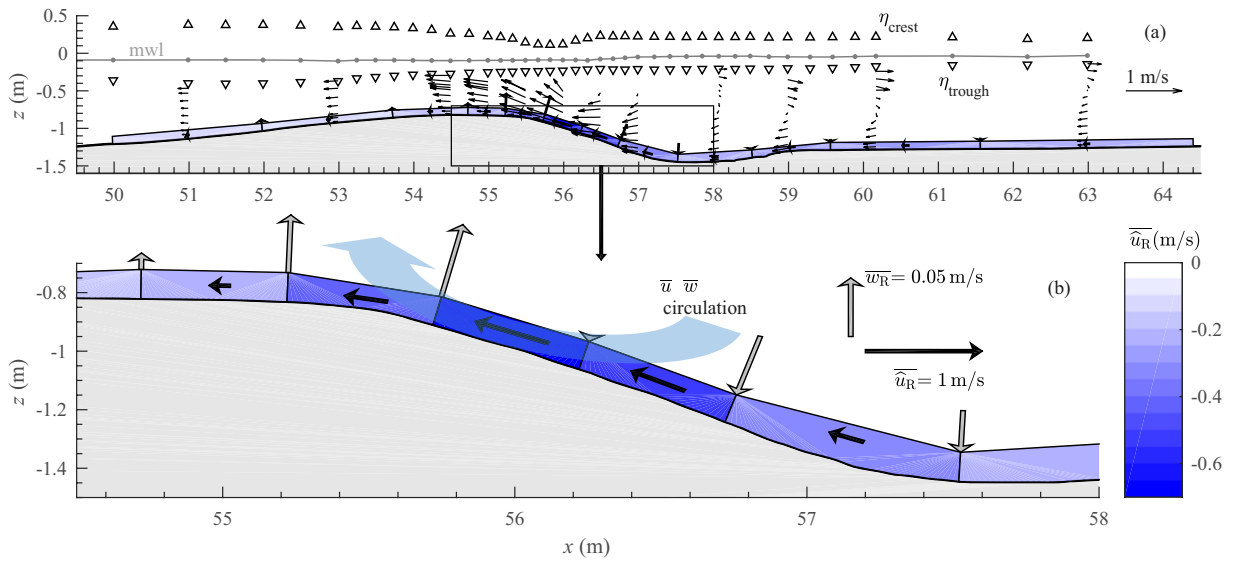

Figure 2. Time-averaged velocities at (a) outer flow and (b) near-bed elevations. Plot (a) shows time-averaged water surface (mwl; dotted line), levels of maximum and minimum phase-averaged water surface (triangles), and 2-dimensional vector field (u, w; arrows). Figure 2b shows time-averaged bed-parallel velocity, depth-averaged over the near-bed control volume (black arrows plus background color indicating magnitude), and bed-normal velocities $\overline{w_{\mathrm{R}}}$ at $\zeta = D$ (grey arrows). The latter data points are averaged over two adjacent cross-shore locations for illustration purposes. The wide curved arrow in Figure 2b illustrates the two-dimensional time-averaged fluid circulation.

secondary waves. These secondary waves modulated wave heights over the offshore slope, but their effect on wave evolution was limited in the breaking and inner surf zones (van der A et al., 2017).

The time-averaged velocity field reveals distinct undertow profiles with negative (offshore-directed) velocities in the lower half of the water column. Undertow magnitudes and profiles vary strongly across the test section, with particularly large magnitudes (up to 0.8 m/s) close to the bed along the shoreward-facing bar slope between bar crest and trough ($x = 55$ to 58 m). The velocity vectors are clearly affected by the bed geometry and partly follow the curvature of the breaker bar. The vectors further reveal a large-scale, wave-averaged fluid circulation between the breaking and inner surf zone, with velocities over the water column directed downward in the inner surf zone ($x > 58.5$ m) and upward above the bar crest ($x = 55.5$ m).

3.2. Near-Bed Flow

The colored rectangles in Figures 2a and 2b depict the near-bed control volumes that are used in section 4 to analyze the TKE budget. The color code and size of the black arrow indicate the magnitude of the near-bed depth-averaged (up to $\zeta = 0.10$ m) undertow velocity $\overline{\widehat{u_R}}$. Undertow magnitudes increase from the shoaling region to the bar crest and continue to increase until a local maximum in $\overline{\widehat{u_R}}$ magnitude is reached along the shoreward-facing bar slope at $x = 56.0$ m. Further shoreward, toward the bar trough, $\overline{\widehat{u_R}}$ decreases in magnitude. Overall, time-averaged bed-parallel velocities show strong cross-shore variation along the barred profile.

Mass conservation requires that the cross-shore gradient in bed-parallel velocities should be balanced by velocities in the bed-normal direction, w_R, i.e., $\overline{w_R}(D) = -{}^{1}/_{D}{}^{d}/_{dx} \int_0^D \overline{u_R} d\zeta$. The latter expression was validated with the measurements, yielding 0.01 m/s accuracy, which supports the applied velocity transformation. Bed-normal velocities $\overline{w_R}$ at $\zeta = D$ are included in Figure 2b (grey arrows), revealing a net fluid flux that is directed away from the bed at the shoaling zone and bar crest ($x = 52$ to 56 m) and toward the bed at the lower section of the shoreward-facing bar slope and the bar trough ($x = 56$ to 59 m), thereby confirming a clockwise fluid circulation through the near-bed layer. Between $x = 52$ and 56 m, $\overline{w_R}(D)$ reaches magnitudes of about 0.05 m/s.

The phase-averaged near-bed horizontal and vertical velocities at seven cross-shore locations are shown at intrawave time scale in Figure 3. For reference throughout the paper, and to facilitate comparison with other studies, the main hydrodynamic parameters corresponding to these locations are presented in Table 1.

Figure 3a shows $\langle u_R(\zeta, t)\rangle$ as contour and Figure 3c shows the vertical profiles of $\bar{u}_R(\zeta)$ (blue) and of $\langle u_R(\zeta)\rangle$ at the phases of minimum and maximum free-stream velocity (black). Although the data at each cross-shore location were obtained from point measurements during different experimental runs, the scatter in the data is limited which indicates good experimental repeatability. At all locations, $\bar{u}_R$ is directed offshore at all elevations and is largely dominated by the undertow: the vertical structures of $\bar{u}_R$ do not reveal evident contributions of other WBL streaming mechanisms (e.g., offshore wave shape streaming, onshore Longuet-Higgins streaming). At $x = 51.0$ m, i.e., before wave breaking, $\bar{u}_R$ is small compared to the periodic velocities $\tilde{u}_R$. The maximum velocity overshoot during the onshore flow half-cycle is found at $\zeta \approx 0.01$ m (Figure 3c); this elevation can be used as an indication of the WBL thickness (Jensen et al., 1989). At $x = 55.0$ m (bar crest), the undertow velocity increases in magnitude, which leads to a decrease in peak onshore and an increase in peak offshore velocity compared to $x = 51.0$ m. At $x = 56.0$ m, the highest undertow magnitudes occur and $\langle u_R\rangle$ is directed offshore for almost the complete wave cycle. Between $x = 57.0$ and 63.0 m, i.e., at the bar trough and the inner surf zone, the undertow weakens and onshore-directed wave crest velocities are restored. At these locations, $\langle u_R\rangle$ is almost depth-uniform, indicating a thin WBL (thickness ≈ 0.005 m).

Figure 3b shows phase-averaged velocities in the bed-normal direction $\langle w_R(\zeta, t)\rangle$. At $x = 51.0$ and 55.0 m, $\langle w_R\rangle$ shows an evident signature of the wave orbital motion, with particularly strong upward $\langle w_R\rangle$ during the zero-up crossing and relatively mild downward $\langle w_R\rangle$ during the zero-down crossing of the strongly asymmetric wave. At $x = 56.0$ m, $\langle w_R\rangle$ is almost continuously directed away from the bed. This location is at the shoreward-facing bar slope where the time-averaged circulation described above leaves the near-bed layer. At $x = 57.0$ m, $\langle w_R\rangle$ is predominantly negative because at this location the time-averaged circulation is toward the bed; a short duration of positive $\langle w_R\rangle$ occurs around the zero-up crossing of the water surface. The behavior of $\langle w_R\rangle$ at $x = 58.1$ to 63.0 m is similar to that at $x = 57.0$ m, but the magnitudes of $\langle w_R\rangle$ are smaller.

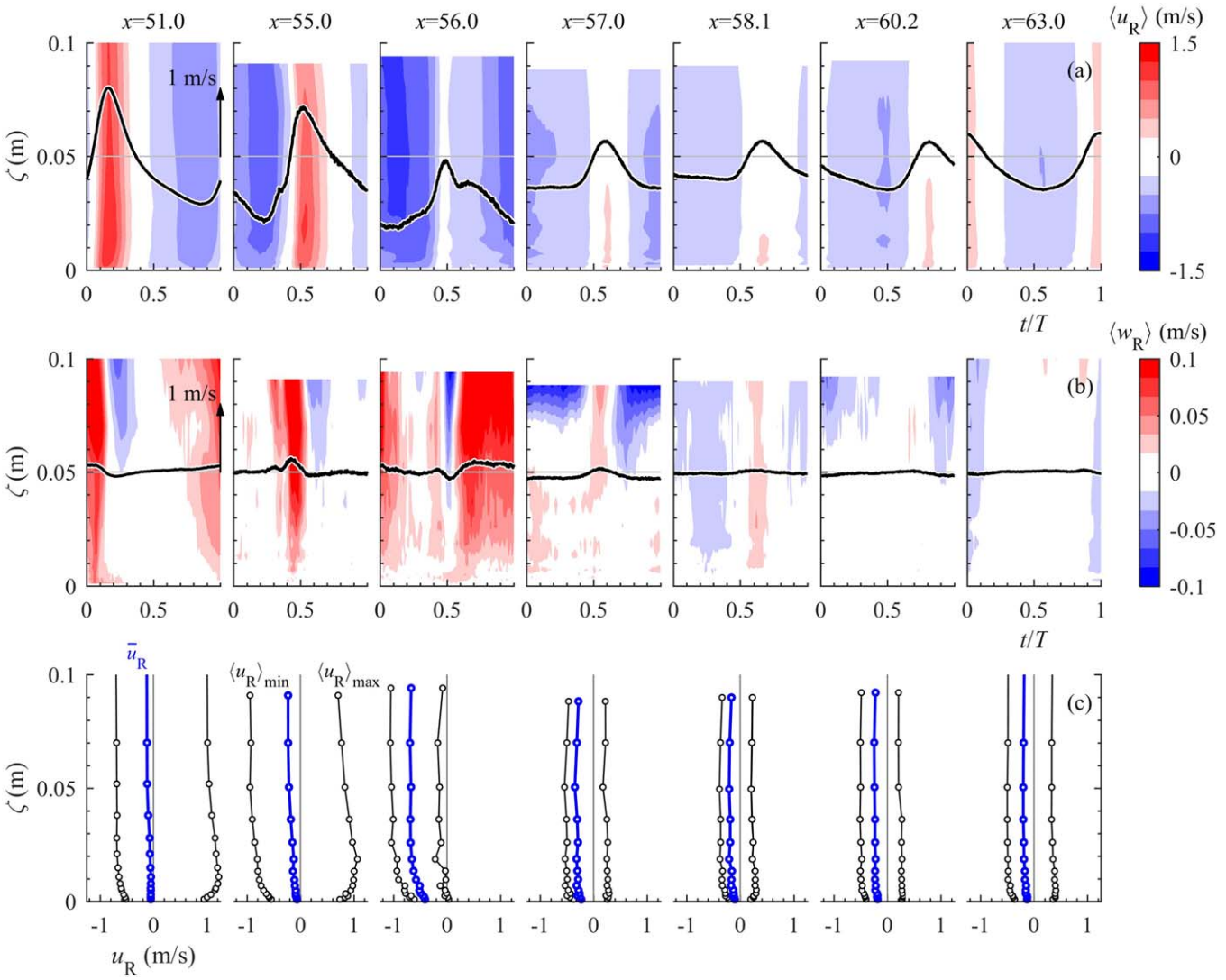

Figure 3. Phase-averaged near-bed velocity. (a) Color contours of bed-parallel velocity $\langle u_R \rangle$, including time series of the free-stream velocity $\langle u_{R,\infty} \rangle$ (black line; arrow in left plot depicts magnitude); (b) as (a), but contours and line now showing velocity in bed-normal direction $\langle w_R \rangle$; (c) Vertical profiles of time-averaged bed-parallel velocity $\bar{u}_R$ (blue) and profiles of $\langle u_R \rangle$ during instant of maximum $\langle u_{R,\infty} \rangle$ in onshore and offshore direction (black). Note the differences in color scale between Figures 3a and 3b.

A remarkable feature in the phase-averaged velocities is the fluid motion induced by the plunging jet, which produces a periodic vortex. By the applied velocity decomposition, the phase-coherent velocities induced by this vortex are part of the periodic velocity components $\langle \tilde{u} \rangle$ and $\langle \tilde{w} \rangle$. The plunging jet induces a short but intense downward and onshore-directed fluid pulse at the front of the wave, which can be clearly observed in outer-flow $\langle \tilde{u} \rangle$ and $\langle \tilde{w} \rangle$ at $x = 55.0$ to 56.0 m (see Figure 8 in van der A et al., 2017). In Figure 3b, the penetration of the plunging jet into the near-bed layer is observed at $x = 56.0$ m at $t/T \approx 0.5$, when $\langle w_R \rangle$ reveals a short-duration negative value, i.e., directed toward the bed. This shows that the periodic plunging wave vortex extends vertically over nearly the full water column.

4. Turbulence

4.1. Outer-Flow TKE and Reynolds Stress

The outer-flow phase-averaged and time-averaged turbulence parameters have been described in detail by van der A et al. (2017). Here we briefly revisit the outer-flow turbulent kinetic energy (k) and time-averaged

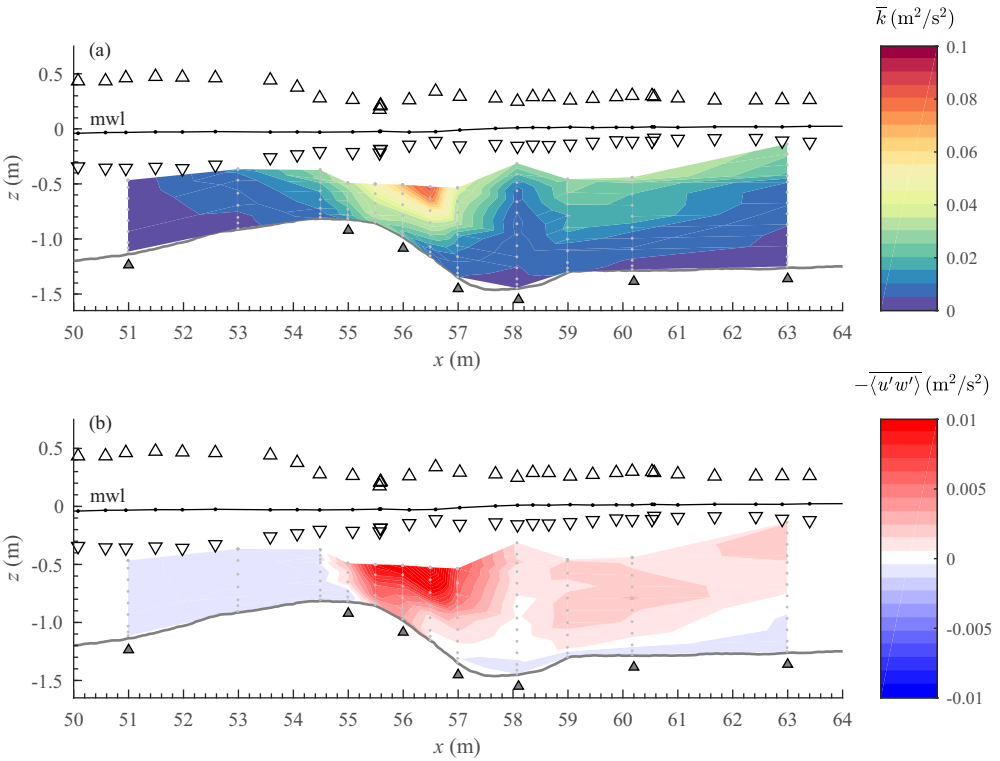

Figure 4. (a) Time-averaged turbulent kinetic energy; (b) time-averaged turbulent Reynolds stress. Open triangles at top mark maximum and minimum phase-averaged water surface. Grey dots indicate the outer-flow velocity measurement positions. Grey triangles at bottom mark the seven cross-shore locations for which detailed WBL velocities were measured.

Reynolds stresses ($-\overline{u'w'}$), as shown in Figure 4, because these are essential for understanding the near-bed turbulence presented in the subsequent sections.

Due to breaking-induced turbulence production, $\overline{k}$ is up to an order of magnitude higher in the breaking region than in the shoaling zone (Figure 4a). High $\overline{k}$ is especially observed above the bar crest, about 1 to 2 m shoreward from the plunge point. This increase in $\overline{k}$ is not restricted to elevations near the water surface, but is also observed at elevations close to the bed. The transport of TKE in the horizontal and vertical directions is mainly by advection: the diffusive transport is almost an order of magnitude lower. Breaking-generated turbulence is transported offshore by the undertow and reaches as far offshore as $x \approx 52$ m, which corresponds to the "break point" where wave breaking commences. A fraction (20–50%) of the breaking-generated TKE decays within a wave cycle; the remainder is still present upon arrival of the subsequent breaking wave (van der A et al., 2017). The correlation between TKE and wave phase at near-bed elevations showed that turbulence at most locations is highest under the wave trough, suggesting that the arrival of breaking-generated TKE at the bed lags its production at the water surface by about $T/2$. However, at the bar crest ($x = 55.0$ to 56.0 m), TKE over the complete water column is highest under the wave crest.

The region with high $\overline{k}$ also shows high values of time-averaged turbulent Reynolds stress $-\overline{u'w'}$ (Figure 4b). Outer-flow Reynolds stresses are positive between $x = 55.0$ and 63.0 m, corresponding to a directional orientation of the breaking-generated vortices that is, on average, downward and onshore, or upward and offshore. In the breaking region, seaward of the bar crest ($x < 55.0$ m), $-\overline{u'w'}$ has much smaller magnitude and has negative sign.

4.2. Near-Bed TKE and Turbulence Intensities

This section presents the near-bed turbulence intensities and TKE at the seven cross-shore locations at which high-resolution LDA velocity measuremenst were obtained. Figures 5a–5g shows color contour plots of $\langle k(\zeta, t) \rangle$, and Figures 5h–5n shows time series of $\langle k(t) \rangle$ at $\zeta = 0.001$ m (blue) and of the depth-averaged near-bed TKE, $\langle \widehat{k}(t) \rangle$ (black).

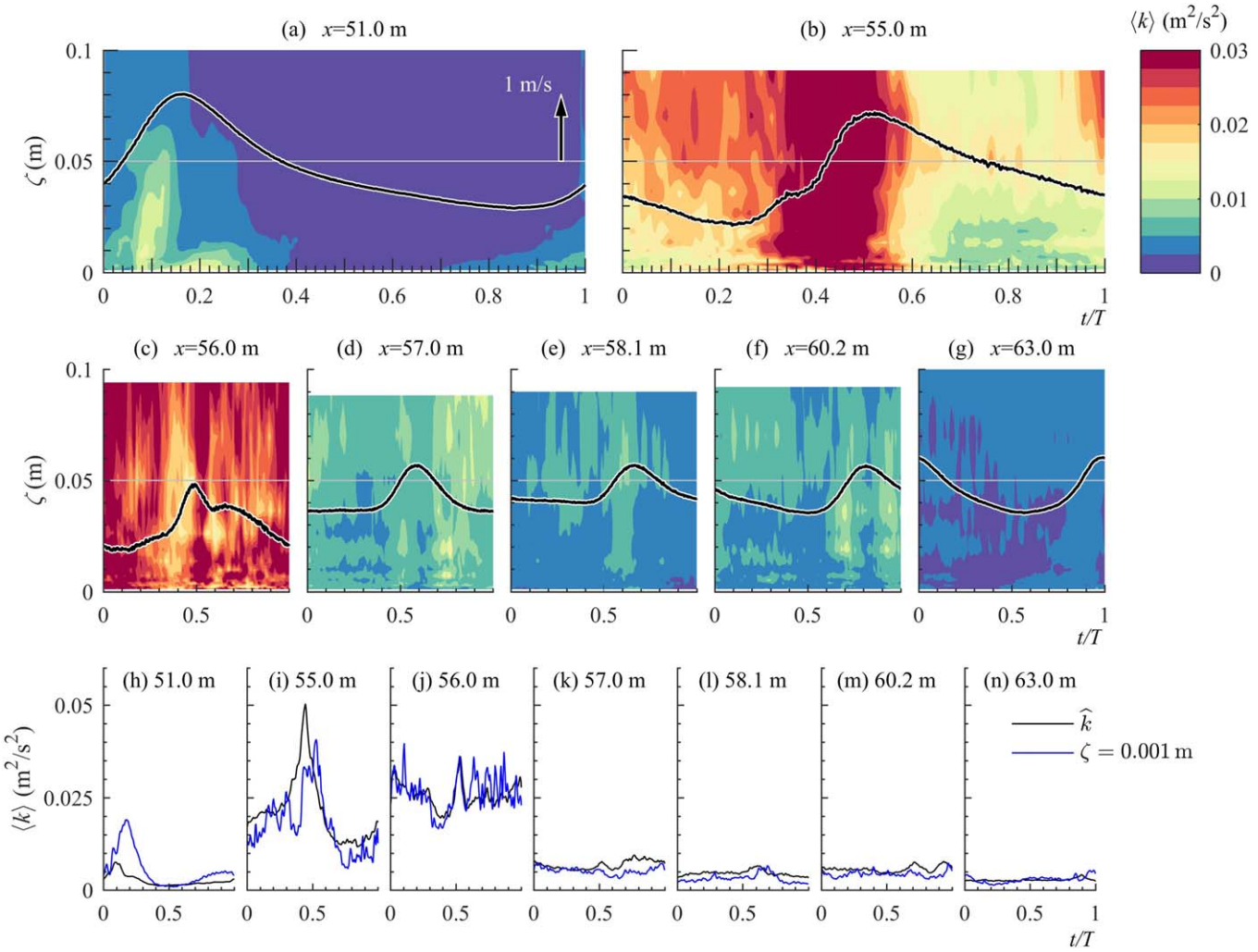

Figure 5. Time series of near-bed phase-averaged TKE. (a)–(g) depth-varying phase-dependent turbulent kinetic energy $\langle k \rangle$ (color contour), with the free-stream bed-parallel velocity $\langle u_{R,\infty} \rangle$ (black line) for reference (arrow in (a) indicates velocity magnitude); (h)–(n) $\langle k \rangle$ at $\zeta = 0.001$ m (blue) and depth-averaged over near-bed control volume (black).

The most offshore located measurement in the shoaling region ($x = 51.0$ m) is not significantly affected by breaking-generated turbulence. At this location, TKE is generated close to the bed during both the onshore (positive) and offshore (negative) flow half-cycles, leading to two maxima in $\langle k \rangle$ at $\zeta = 0.001$ m that are approximately in phase with the maximum onshore ($t/T = 0.17$) and maximum offshore ($t/T = 0.87$) free-stream velocity (Figure 5h, blue line). At $\zeta = 0.001$ m, the maximum $\langle k \rangle$ during the onshore half-cycle (0.019 m^2/s^2) exceeds the maximum $\langle k \rangle$ during the offshore half-cycle (0.005 m^2/s^2) by more than a factor of 3. At such close proximity to the bed, $\langle k \rangle$ is expected to scale with $\langle u_\infty \rangle^2$ (e.g., Hinze, 1975). Based on velocity skewness, maximum $\langle u_\infty \rangle^2$ during the onshore half-cycle exceeds $\langle u_\infty \rangle^2$ during the offshore half-cycle by a factor 2. The even higher difference (factor 3) in $\langle k \rangle$ between both half cycles may therefore be due to positive acceleration skewness, which also contributes to higher bed friction and turbulence production during the onshore half-cycle (van der A et al., 2011). The turbulence generated during the offshore half-cycle appears to spread upward to $\zeta > 0.05$ m under the wave front ($t/T \approx 0$ to 0.1; Figure 5a). This vertical spreading is partly due to advection by the upward-directed periodic velocities under the wave front. However, as will be shown in section 4.6, intrawave cross-shore advection by the periodic velocity also contributes to high TKE under the wave fronts of the propagating waves. In contrast to the offshore half-cycle, the turbulence generated during the onshore half-cycle remains confined to a distance close to the bed ($\zeta < 0.02$ m), since $\langle w_R \rangle$ is directed toward the bed under the rear of the wave (Figure 5a, $t/T = 0.2$ to 0.6).

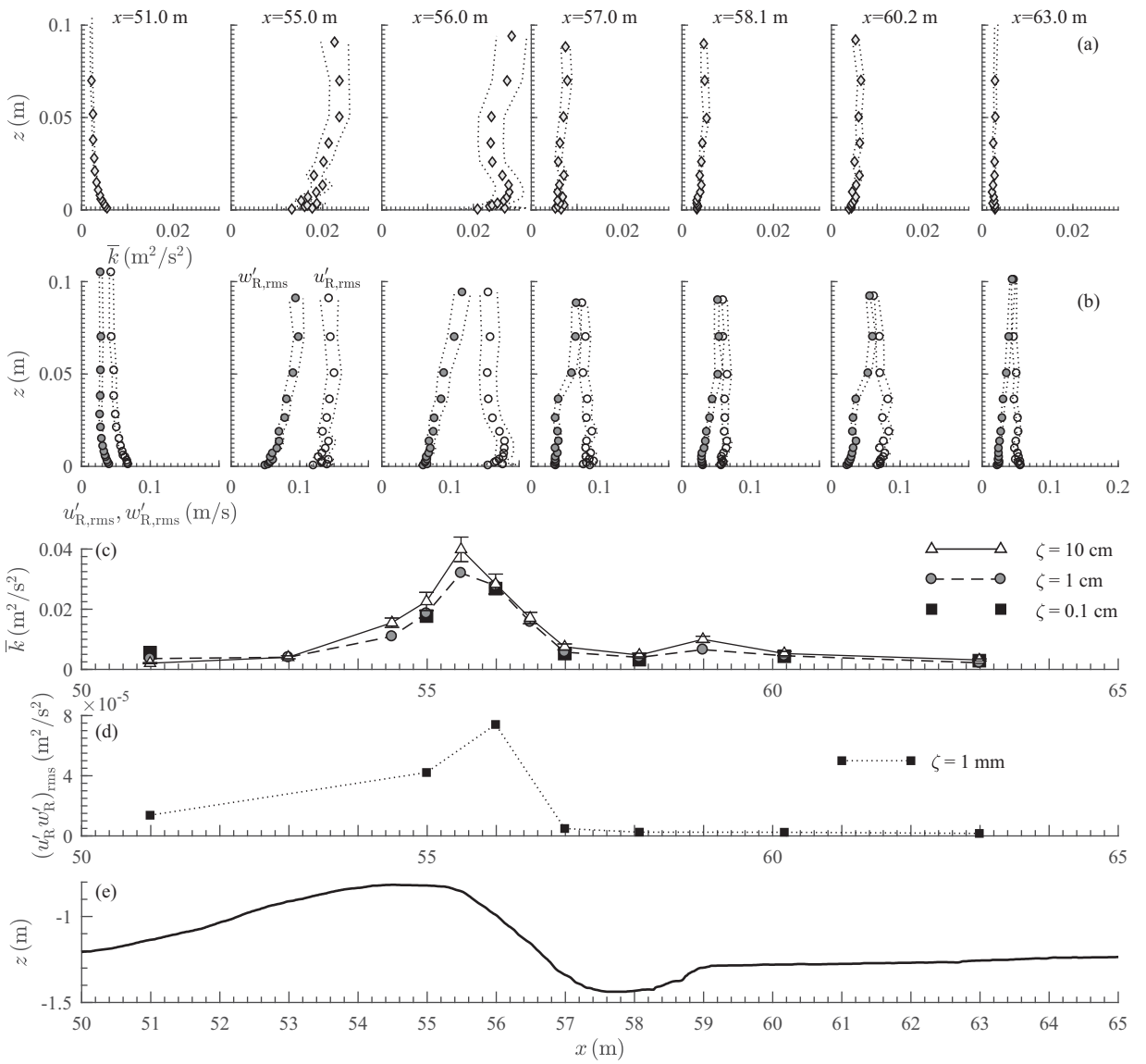

Figure 6. Time-averaged turbulence quantities. (a) Vertical profiles of time-averaged turbulent kinetic energy; (b) Vertical profiles of turbulence intensities $u'_{R,rms}$ (white) and $w'_{R,rms}$ (grey) at seven locations; (c) Time-averaged turbulent kinetic energy at three elevations, i.e., $\zeta \approx 0.10$ m (solid line and grey squares), $\zeta \approx 0.01$ m (dashed line and white triangles), $\zeta \approx 0.001$ m (dotted line and black circles); (d) Root-mean-square turbulent Reynolds stress $\sqrt{\overline{(u'_R w'_R)^2}}$ at $z - z_{bed} = 1$ mm; and (e) Bed profile. Dotted lines in Figures 6a and 6b and error bars in Figure 6c indicate 95% confidence-interval.

The depth-averaged TKE $\langle \widehat{k} \rangle$ (Figure 5h, black line) is highest at $t/T = 0.1$, slightly lagging the zero-crossing of $\langle u_{R,\infty} \rangle$ at $t/T = 0.05$.

The behavior of near-bed TKE is notably different at $x = 55.0$ m, which is at the bar crest and about 0.5 m shoreward from the plunge point. TKE increases rapidly and at all elevations under the wave front, i.e., starting during the deceleration phase of the offshore half-cycle ($t/T = 0.3$) and continuing during the accelerating stage of the onshore half-cycle (until $t/T = 0.45$). Note that the TKE increase commences slightly before the plunging jet strikes the water surface ($t/T = 0.35$) and arrives at the bottom ($t/T = 0.50$; Figure 3b), so this increase is not explained by a direct turbulence influx by the plunging jet from above. The latter is confirmed by the upward-directed free-stream velocity ($\langle w_{R,\infty} \rangle > 0$) during the stage of TKE increase ($t/T = 0.3$ to 0.45). Instead, this increase is primarily caused by local turbulence production and a bed-parallel TKE influx from shoreward locations, as will be explained in sections 4.4 and 4.6. TKE decreases during the remainder of the onshore half-cycle ($t/T = 0.45$ to 0.7) and increases gradually during the beginning of the offshore half-cycle (from $t/T = 0.75$ to 0.30 in next half-cycle), especially at $\zeta > 0.05$ m (Figure 5b).

At $x = 56.0$ m $\langle k \rangle$ is almost depth-uniform and is continuously high, with slightly greater values during the onshore than during the offshore half-cycle. Further shoreward ($x = 57.0$ m), TKE magnitudes are significantly lower. Here, $\langle k \rangle$ increases slightly during the onshore-to-offshore velocity reversal ($t/T = 0.65$), when $\langle w_R \rangle$ is directed toward the bed. The measurement locations at the bar trough and inner surf zone between $x = 58.1$ to 63.0 m generally reveal limited temporal variation and vertical structure in $\langle k \rangle$.

Figure 6 shows vertical profiles of time-averaged TKE ($\overline{k}$; plot (a)) and of bed-parallel and bed-normal turbulence intensities ($u'_{R,rms}$ and $w'_{R,rms}$; plot (b)). The 95% confidence intervals were calculated based on the turbulence time series, taking into account the nonnormal distribution of these turbulence parameters (Benedict & Gould, 1996). At $x = 51.0$ m, turbulence intensities and $\overline{k}$ are largest close to the bed and decrease upward, as expected for a rough-bed oscillatory boundary layer where bed shear is the primary source of turbulence generation (e.g., Sleath, 1987; van der A et al., 2011). Turbulence is anisotropic with a ratio $w'_{R,rms}/u'_{R,rms} \approx 0.5$, consistent with boundary layer measurements (e.g., Jensen et al., 1989; Sleath, 1987) and Svendsen's (1987) proposed value for boundary layer turbulence (outer region). The latter also justifies the factor 1.47 in equation (5) to calculate $\langle k \rangle$.

In contrast, at $x = 55.0$ m and $x = 56.0$ m, $\overline{k}$ and turbulence intensities increase from the bed upward. Such an upward increase cannot be explained by local bed shear production only and marks the combined effect of external turbulence that arrives at these locations and local turbulence production, as will be explored in detail in the next sections. The wave breaking vortices at these locations are compressed in the vicinity of the bed, which explains why $w'_{R,rms}$ reduces more rapidly than $u'_{R,rms}$ toward the bed (Figure 6b). Consequently, turbulence in the near-bed layer is strongly anisotropic ($u'_{R,rms} > w'_{R,rms}$). The $\overline{k}(\zeta)$ profile at $x = 56.0$ m shows a distinct structure with a local maximum near $\zeta = 0.01$ m and a depression near $\zeta = 0.04$ m (Figure 6a). This could be attributed to separate contributions by the two turbulence sources, being wave breaking, and bed shear stress, leading to a local "bottleneck" in the near-bed TKE profile (Justesen et al., 1987).

From $x = 57.0$ to 63.0 m, free-stream turbulence at $\zeta = 0.10$ m is roughly isotropic ($w'_{R,rms}/u'_{R,rms} \approx 1$), but also here, turbulence becomes increasingly anisotropic toward the bed. At these locations, $\overline{k}(\zeta)$ is almost depth-uniform over the complete near-bed layer.

Figure 6c shows the cross-shore variation of time-averaged TKE at three elevations. At all elevations, $\overline{k}$ increases significantly between the shoaling ($x = 51.0$ m) and breaking regions. $\overline{k}$ is highest at $x = 56.0$ m, which is on the shoreward-facing bar slope, about 1.5 m shoreward from the plunge point. The increase in TKE is not restricted to elevations far from the bed, since also at $\zeta = 0.001$ m $\overline{k}$ increases (by a factor 5 from $x = 51.0$ to 56.0 m). Note further that $x = 51.0$ m (shoaling zone), albeit difficult to see on this scale, is the only location where $\overline{k}$ is higher close to the bed (at $\zeta = 0.001$ m) instead of at the free-stream elevation ($\zeta = 0.10$ m). At the bar trough and inner surf zone ($x \geq 58.1$ m), $\overline{k}$ is substantially lower than in the breaking region and has similar magnitude as $\overline{k}$ in the shoaling zone ($x = 51.0$ m).

4.3. Turbulent Reynolds Stress

Figure 7a shows the phase-averaged turbulent Reynolds stress $-\langle u'_R w'_R \rangle$. At $x = 51.0$ m the Reynolds stress is consistent with the results for $\langle k \rangle$ at the same location (Figure 6). Here $-\langle u'_R w'_R \rangle$ is highest at the bed, where it is in phase with $\langle u_{R,\infty} \rangle$, showing peak values at times of maximum onshore and offshore free-stream velocity. With distance from the bed, $-\langle u'_R w'_R \rangle$ decreases in magnitude and shows an increasing phase lag with respect to $\langle u_{R,\infty} \rangle$. Such temporal behavior is consistent with previous boundary layer observations of $-\langle u'_R w'_R \rangle$ in oscillatory flow tunnel (Jensen et al., 1989; Sleath, 1987; van der A et al., 2011) and small-scale wave flume (Henriquez et al., 2014) experiments. Note that the negative Reynolds stress, corresponding to turbulence generated during the offshore half-cycle, persists well into the onshore half-cycle ($\zeta \approx 0.02$ m, $t/T \approx 0.2$). This behavior has been observed before for oscillatory boundary layers in acceleration-skewed flows and is due to the relatively short time between maximum negative velocity and the negative-positive reversal (van der A et al., 2011).

At $x = 55.0$ m (bar crest), the temporal and vertical structure of $-\langle u'_R w'_R \rangle$ for elevations close to the bed ($\zeta < 0.02$ m) is similar to that at $x = 51.0$ m, suggesting that the Reynolds stresses close to the bed at this x are primarily determined by the local bed shear-produced turbulence. At $\zeta > 0.02$ m, $-\langle u'_R w'_R \rangle$ is predominantly negative, which is consistent with the negative $-\overline{u'w'}$ observed at outer-flow elevations (Figure 4).

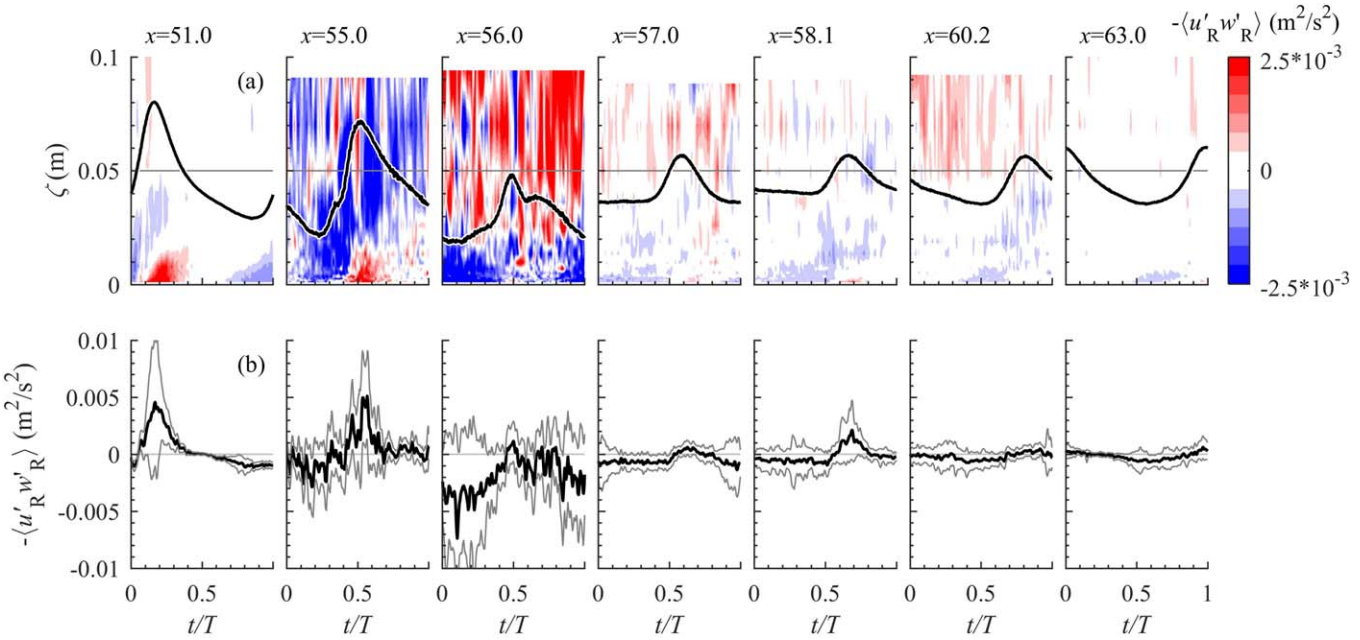

Figure 7. Phase-averaged turbulent Reynolds stress $-\langle u'_R w'_R \rangle$. (a) Depth-varying phase-dependent turbulent Reynolds stress (color contour), with the free-stream bed-parallel velocity $\langle u_{R,\infty} \rangle$ (black line) for reference; (b) phase-averaged Reynolds stress at $\zeta = 0.001$ m (black) ± 1 standard deviation (grey).

The negative $-\langle u'_R w'_R \rangle$ could relate to the offshore-directed undertow, which produces a negative velocity shear ($d\bar{u}_R/d\zeta < 0$) and hence negative $-\langle u'_R w'_R \rangle$ by current-related bed shear on average. Alternatively, the negative $-\langle u'_R w'_R \rangle$ may be associated with breaking-generated vortices: although these vortices have a preferential orientation corresponding to a positive Reynolds stress in the region with highest outer-flow TKE (Figure 4b), their orientation may change whilst being convected downward and offshore over the breaker bar by the rotational plunging vortex and the undertow.

At $x = 56.0$ m on the shoreward slope of the bar, the Reynolds stress is mostly positive for $\zeta > 0.02$ m, which is consistent with the positive $-\overline{u'w'}$ at outer-flow elevations and is due to breaking-generated turbulence. Close to the bed, the sign of $-\langle u'_R w'_R \rangle$ changes from positive ($\zeta > 0.02$ m) to negative ($\zeta < 0.02$ m). As for $x = 55.0$ m, the negative Reynolds stress at $\zeta < 0.02$ m can be explained by bed-shear-generated turbulence, which is expected to produce negative $-\langle u'_R w'_R \rangle$ due to the strong offshore-directed undertow. Further shoreward ($x = 57.0$ to 63.0 m), the magnitudes of $-\langle u'_R w'_R \rangle$ decrease. Negative Reynolds stress is produced at the bed during the offshore half-cycle and spreads upward, while the positive Reynolds stress at higher elevations is associated with breaking-generated turbulence.

Figure 7b shows the time series of $-\langle u'_R w'_R \rangle$ very close to the bed ($\zeta = 0.001$ m). The ± standard deviation of $-\langle u'_R w'_R \rangle$, included as grey lines, provides an estimate of the magnitude of the instantaneous Reynolds stress $-u'_R w'_R$. At all locations, $-\langle u'_R w'_R \rangle$ corresponds well with the free-stream velocity $\langle u_{R,\infty} \rangle$ in terms of sign and phase behavior. Consequently, the presence of wave breaking turbulence in the WBL at some locations (especially at $x = 55.0$ and 56.0 m) appears to have no effect on the phase-averaged Reynolds stresses $-\langle u'_R w'_R \rangle$ at $\zeta = 0.001$ m.

However, the *instantaneous* Reynolds stress magnitudes vary strongly between different x-locations, which can be most prominently seen in the overall much higher standard deviations at $x = 55.0$ and 56.0 m compared to $x = 51.0$ m (grey lines in Figure 7b). The cross-shore variation is further examined through Figure 6d, which shows the root-mean-square Reynolds stresses $\left(u'_R w'_R\right)_{rms} = \overline{\left(u'_R w'_R\right)^2}^{1/2}$ along the bar. Figure 6d reveals a factor 5 increase in $\left(u'_R w'_R\right)_{rms}$ from the shoaling ($x = 51.0$ m) to the breaking region (at $x = 56.0$ m), followed by a strong decrease at the bar trough and inner surf zone—a pattern that is consistent with $\bar{k}(\zeta = 0.001$ m). The increase in instantaneous Reynolds stress magnitudes can be explained by the intermittent (i.e., uncorrelated with wave phase) arrival of breaking-generated turbulence at the bed, as explained by Cox and Kobayashi (2000) based on similar observations under small-scale spilling breakers.

4.4. Turbulence Production Rate

Equation (10) shows that the turbulence production has a shear stress contribution $\mathcal{P}_s \approx -\langle u'_R w'_R \rangle \partial\langle u_R \rangle/\partial z$ and a normal stress contribution $\mathcal{P}_n = \left[\langle w'^2_R \rangle - \langle u'^2_R \rangle\right] \partial\langle w_R \rangle/\partial z$. Shear production $\mathcal{P}_s$ will contribute particularly when the velocity shear $\partial\langle u_R \rangle/\partial z$ is high, i.e., at elevations close to the bed (inside the WBL) and at times of peak onshore/offshore velocity. The normal stress term contributes only when the flow is nonuniform, i.e., $\partial\langle w_R \rangle/\partial z = -\partial\langle u_R \rangle/\partial x \neq 0$. The latter is always true under progressive surface waves where the periodic velocity field changes in time and space, leading to horizontal flow convergence, and upward velocities under the wave front and horizontal flow divergence, and downward velocities under the wave rear. For the present strongly asymmetric waves, the spatial velocity gradients ($\partial\langle u_R \rangle/\partial x$, $\partial\langle w_R \rangle/\partial z$) are particularly high under the steep wave front, where the converging bed-parallel flow yields high convective accelerations in the horizontal and vertical directions. The bar geometry further contributes to cross-shore variations in undertow ($\partial\langle \overline{u}_R \rangle/\partial x$) and orbital velocities.

Figure 8a shows vertical profiles of the time-averaged production $\overline{\mathcal{P}}$, including the contributions from $\mathcal{P}_s$ and $\mathcal{P}_n$ (note the different scales on the horizontal axes). Figure 8b shows vertical and temporal distributions of the phase-averaged production rate $\langle \mathcal{P} \rangle = \langle \mathcal{P}_s \rangle + \langle \mathcal{P}_n \rangle$. At $x = 51.0$ m turbulence production is predominantly due to $\mathcal{P}_s$. For both half-cycles, turbulence production is initiated at the bed ($\zeta < 0.01$ m) during the accelerating flow stages, when it is in phase with the free-stream velocity magnitude. As soon as the free-stream velocity starts to decelerate ($t/T = 0.90$ in the offshore half-cycle and $t/T = 0.15$ in the onshore half-cycle) and the Reynolds stress diffuses upward, $\langle \mathcal{P} \rangle$ increases at higher elevations. Moving away from the bed, $\langle \mathcal{P} \rangle$ increasingly lags the free-stream velocity magnitude. The temporal and vertical behavior of $\langle \mathcal{P} \rangle$ is qualitatively similar to smooth bed numerical simulations of sinusoidal oscillatory flows by Pedocchi et al. (2011) and Vittori and Verzicco (1998), although the present study shows a strong asymmetry in $\langle \mathcal{P} \rangle$ between the onshore and offshore half cycles due to the skewed-asymmetric nature of the flow and due to progressive surface wave effects.

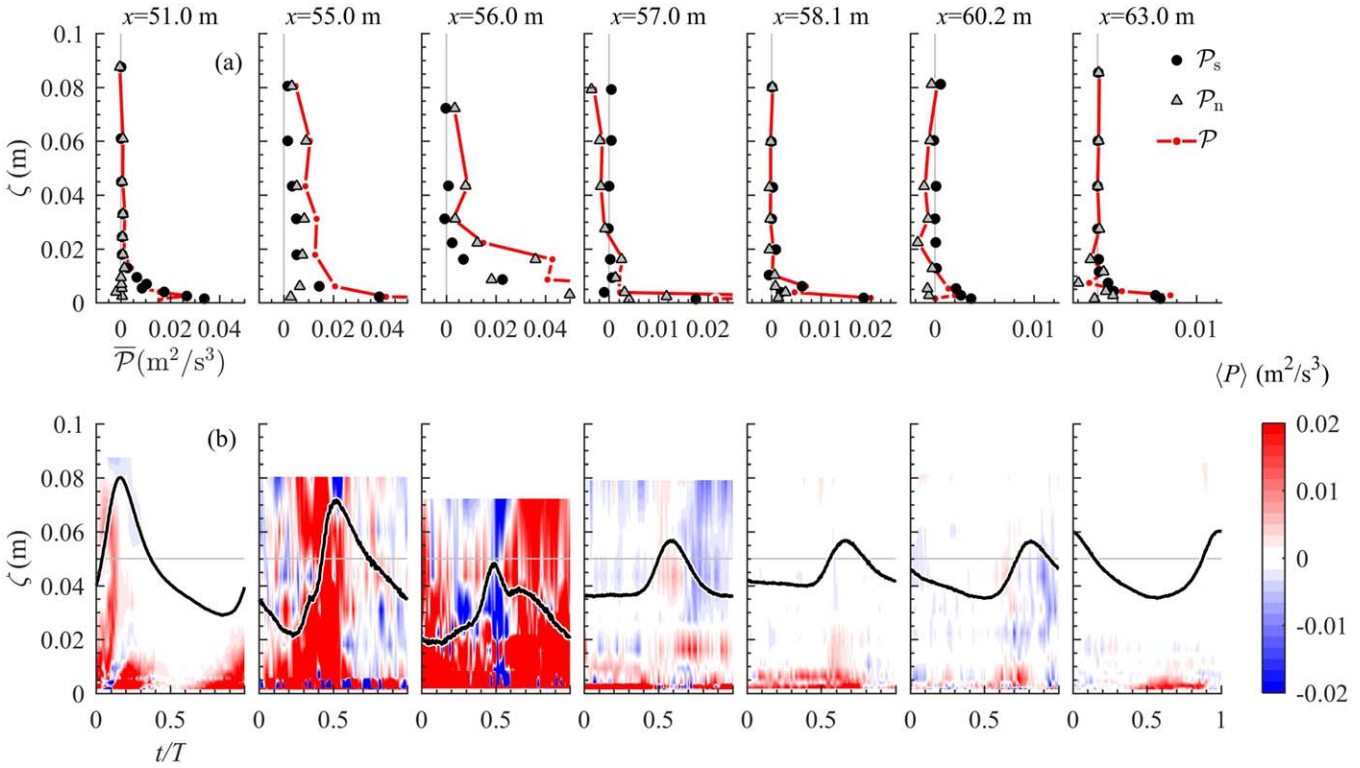

Figure 8. Turbulent production rates. (a) Time-averaged production, contribution by shear stresses (black diamond), contribution by normal stresses (grey triangle), and sum of both contributions (red dots and line; note the different scales for the horizontal axes); (b) Phase-averaged production $\mathcal{P}$ as color contour, including free-stream bed-parallel velocity $\langle u_{R,\infty} \rangle$ (black line) and $\langle u_{R,\infty} \rangle = 0$ (grey line) for reference.

At $x = 55.0$ m, turbulence production magnitudes are much greater than at $x = 51.0$ m, especially at elevations further away from the bed. Both production terms $\mathcal{P}_s$ and $\mathcal{P}_n$ contribute significantly to $\overline{\mathcal{P}}$ (Figure 8a). The significant production by $\mathcal{P}_n$ is due to the presence of energetic anisotropic turbulence at this location (section 4.2). $\langle\mathcal{P}\rangle$ is consistently high, but largest production rates occur under the wave front ($t/T = 0.3$ to 0.6; Figure 8b). Within this time, the high convective acceleration and the relatively high degree of flow nonuniformity lead to turbulent production by the anisotropic turbulent vortices through normal stresses ($\mathcal{P}_n$). This local production of TKE is expected to contribute significantly to the observed increase in $\langle k\rangle$ during the same phase (cf., Figure 5b).

Strong production by $\mathcal{P}_s$ and $\mathcal{P}_n$ is also observed at $x = 56.0$ m. Close to the bed, inside the WBL ($\zeta < 0.02$ m), $\langle\mathcal{P}\rangle$ is continuously high due to the strong shear $\partial\overline{u}_R/\partial\zeta$ by the undertow. At higher elevations, $\langle\mathcal{P}\rangle$ shows more time variation, with highest values under the rear of the wave, i.e., after the passage of the wave crest ($t/T = 0.6$ to 1.0). This turns out to be mainly due to high $\langle\mathcal{P}_n\rangle$, which is again explained by the combination of anisotropic turbulence and convective fluid accelerations. At $x = 56.0$ m these convective accelerations are not so much driven by the orbital velocity, but instead, by the strong cross-shore undertow velocity gradients at this location ($\partial\overline{u}_R/\partial x < 0$; $\partial\overline{w}_R/\partial\zeta > 0$) (Figure 2). Note that the high contributions of $\langle\mathcal{P}_n\rangle$ mark a distinct difference from observations by Ting and Kirby (1995), who found this term to be negligible under small-scale plunging waves over a plane-sloping bed.

Further shoreward ($x = 57.0$ to 63.0 m), $\overline{\mathcal{P}}$ is largely restricted to the lowest 0.01 m, i.e., inside the WBL, and is mostly induced by shear stress. Turbulence production is highest during the offshore half-cycle, because the velocity shear magnitude $|\partial\langle u_R\rangle/\partial\zeta|$ exceeds the shear during the onshore half-cycle. Note that small but consistent negative production rates are locally observed ($x = 57.0$ and 60.2 m) for $\zeta > 0.05$ m (Figure 8a). Negative production rates indicate that kinetic energy is transferred from turbulent motions to the mean velocity field (Tennekes & Lumley, 1972) and can occur when the mean flow field changes or when turbulence is advected to a region with a different mean velocity shear distribution. Observations by Clavero et al. (2016) for plunging waves also highlighted the occurrence of $\langle\mathcal{P}\rangle < 0$, for a short duration under the wave front. In the present study, the negative turbulence production is induced by normal stresses ($\mathcal{P}_s \approx 0$) and occurs mainly under the wave rear. During this stage, anisotropic breaking-generated turbulence is vertically advected by orbital and wave-averaged velocity from free-stream elevations toward the bed ($\langle w_{R,\infty}\rangle < 0$), where the flow is deflected in the offshore direction ($\partial\langle w_R\rangle/\partial\zeta < 0$; $\partial\langle u_R\rangle/\partial x > 0$).

4.5. Turbulence Dissipation Rate

The estimates of ε presented here (using equations (12) and (13)) are subject to important assumptions regarding the relation between ε and measured autospectra of velocities (section 2.5). Consequently, of all TKE budget terms discussed herein, the dissipation rate has the largest expected uncertainty. Previous studies have acknowledged difficulties in quantifying ε in the surf zone; different methods generally produce estimates with consistent qualitative behavior and same order of magnitude, but values may differ by up to a factor of 4 (Bryan et al., 2003; Feddersen et al., 2007; Veron & Melville, 1999). Note that time-averaged dissipation rates $\overline{\varepsilon}$ (computed following Trowbridge & Elgar, 2001) for the outer-flow elevations of the present experiment were shown to be qualitatively and quantitatively consistent with previous surf zone observations (van der A et al., 2017).

Vertical profiles of time-averaged dissipation rate $\overline{\varepsilon}(\zeta)$ are presented in Figure 9a. Note that the horizontal axes have the same scales as in Figure 8a (showing $\overline{\mathcal{P}}(\zeta)$) to facilitate comparison with production rates. Figure 9a shows $\overline{\varepsilon}(\zeta)$ for both applied methods, i.e., equations (12) and (13). The two methods yield $\overline{\varepsilon}$ values that are qualitatively consistent, but quantitatively, $\overline{\varepsilon}$ estimates by equation (13) are approximately twice as high as those calculated using equation (12). The difference is largest at the most offshore location ($x = 51.0$ m). This location is characterized by strong periodic velocities and a relatively weak undertow (high $\tilde{u}_{rms}$, low $\bar{u}$). The difference in $\overline{\varepsilon}$ estimates may be found in the assumption of sinusoidal orbital velocities in the derivation of equation (13) (Lumley & Terray, 1983; Trowbridge & Elgar, 2001), which is violated when applying the method to the present strongly skewed-asymmetric waves.

Both methods however yield a consistent vertical and horizontal variation in $\overline{\varepsilon}(\zeta)$. Dissipation rates are highest in the breaking region at $x = 56.0$ m, where the maximum TKE was also observed. At each location, $\overline{\varepsilon}(\zeta)$ is upward concave with highest values close to the bed, inside the WBL ($\zeta < 0.01$ m). Note that $\overline{\varepsilon}(\zeta)$ shows more vertical variation than $\overline{k}(\zeta)$ (cf., Figure 6a). The high dissipation rates at the bed for approximately

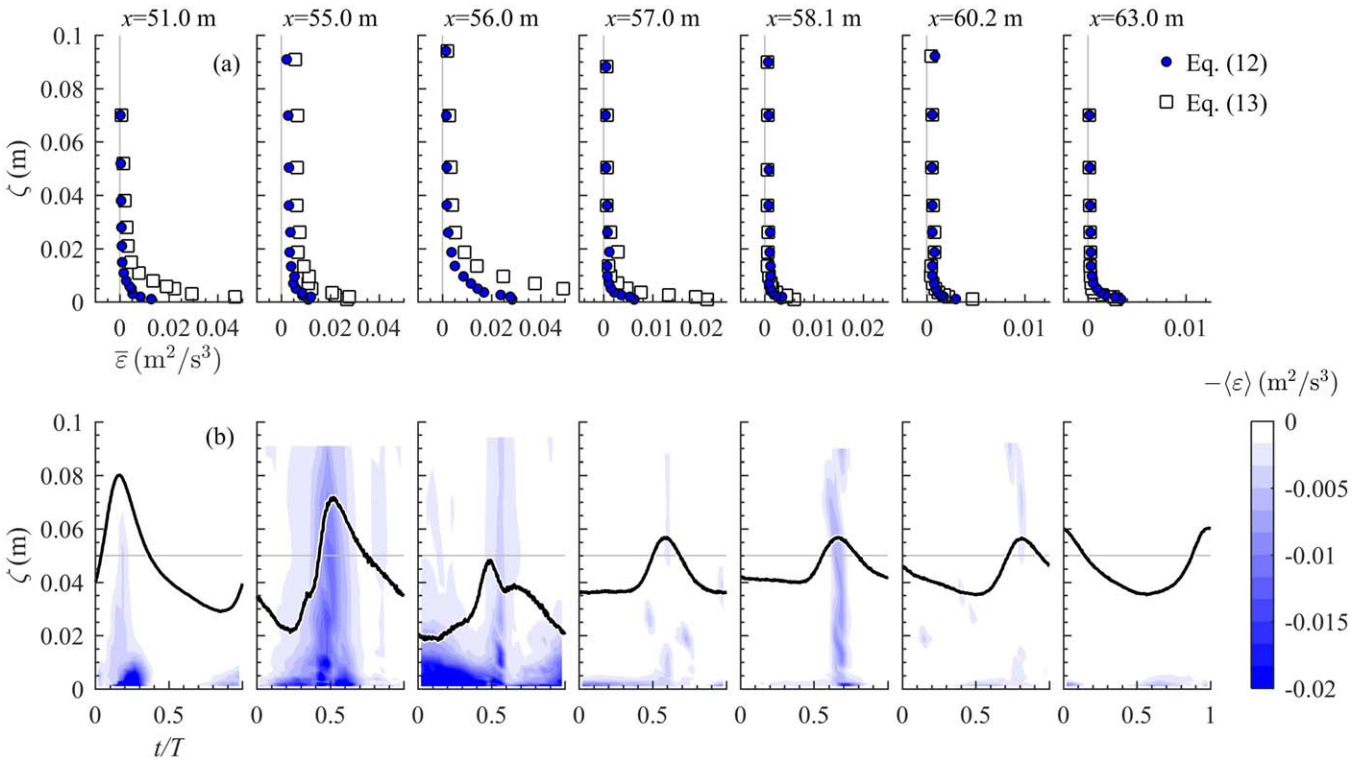

Figure 9. Turbulence dissipation rates. (a) Time-averaged dissipation, calculated through equation (12) (circles) and calculated through equation (13) (squares; note the different scales for the horizontal axes); (b) Phase-averaged dissipation as color contour, calculated through equation (12), with black line indicating free-stream velocity for reference.

depth-uniform $\overline{k}(\zeta)$ is explained by the restricted size of vortices in the vicinity of the bed: ε scales to the inverse of the typical turbulence length scale (e.g., Pope, 2000). The vertical $\overline{\varepsilon}(\zeta)$ profiles are consistent with production rate profiles $\overline{\mathcal{P}}(\zeta)$ (Figure 8a). This is particularly true in the shoaling zone ($x = 51.0$ m) and at the bar trough and inner surf zone locations ($x = 57.0$ to 63.0 m), indicating that at these locations the locally produced TKE is approximately in equilibrium with dissipation. However, in the breaking region around the bar crest ($x = 55.0 - 56.0$ m) the production rates exceed the dissipation rates, i.e., both terms are not in local equilibrium. This leads to a net outgoing flux of TKE from these locations, as discussed in section 4.6.

For completeness Figure 9b shows the phase-averaged dissipation rate $\langle\varepsilon\rangle$. At all locations, the temporal behavior of $\langle\varepsilon\rangle$ is consistent with the behavior of $\langle k\rangle$ (Figure 5), showing that dissipation rates relate directly to TKE.

4.6. TKE Transport

This section presents the horizontal and vertical transport of TKE as advection and diffusion. The present analysis focuses on the complete depth-integrated near-bed layer and does not address the depth-dependent TKE fluxes. In order to relate the spatial and temporal variation of TKE to horizontal and vertical turbulence transport, the data are presented as color contours that represent the spatiotemporal domain (Figure 10). Each of the plots (a)–(f) shows the cross-shore location on the horizontal axis and the normalized time on the vertical axis. Waves propagate through the domain from the lower left corner to the upper right corner. Each plot includes the zero crossings of the water surface for phase reference (dotted lines). A similar presentation of data was used by van der Zanden et al. (2016, 2017a) to study the spatiotemporal variation in breaking-generated turbulence and suspended sediment over a mobile sand bed; their analyses are here extended by quantifying the horizontal and vertical influx of TKE.

Figure 10a shows the depth-averaged bed-parallel velocity $\langle\widehat{u_R}\rangle$. The black arrows show the direction of $\langle\widehat{u_R}\rangle$ during two instants, illustrating how the flow convergences under the wave front ($t/T = 0.24$) and diverges under the wave rear ($t/T = 0.55$). During the onshore half-cycle (between the dotted lines),

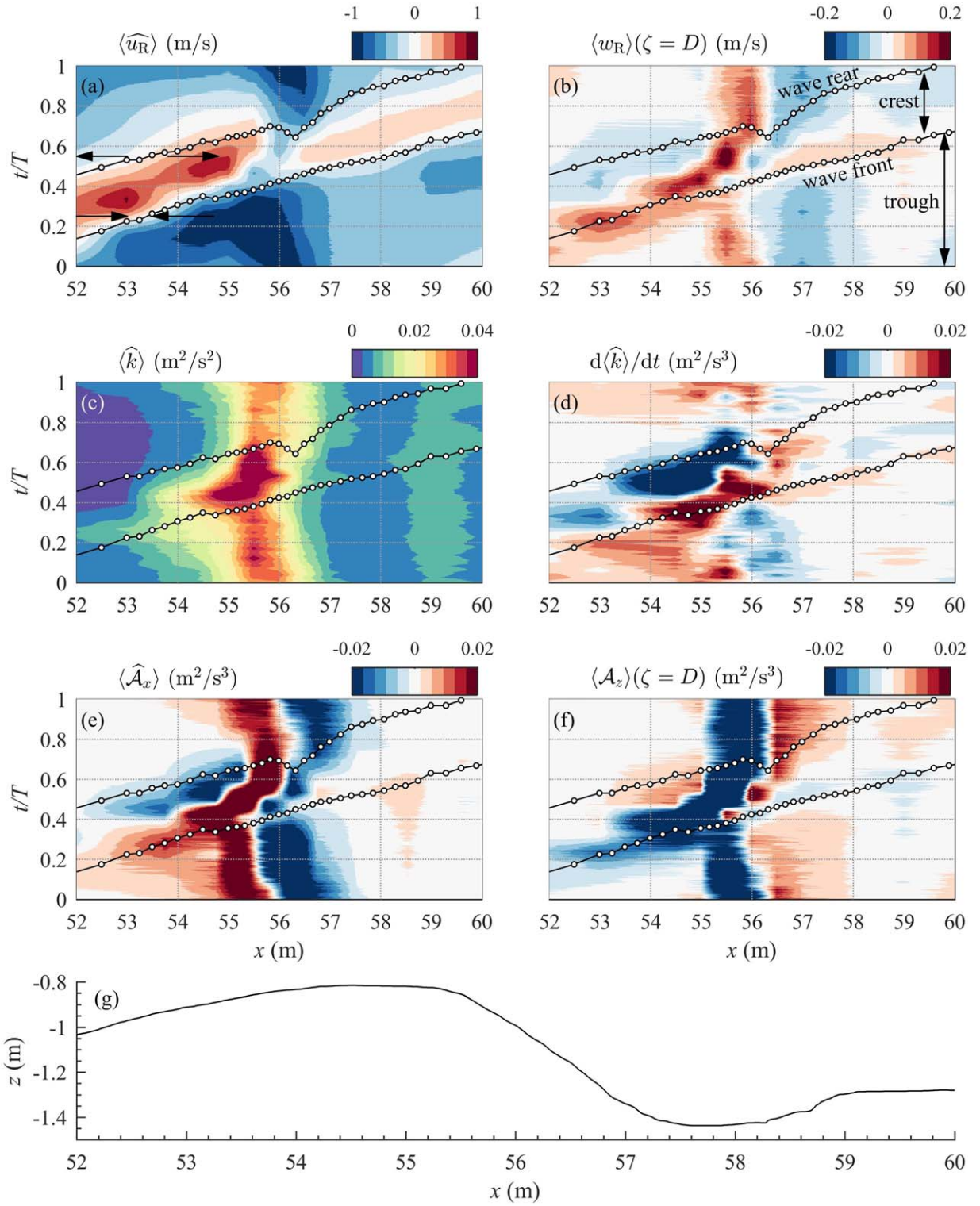

Figure 10. Spatiotemporal variation of velocities, TKE, and advective influx of TKE. Each of plots (a)–(f) shows the spatial domain on the horizontal axis and the temporal domain on the vertical axis. The color contours depict: (a) Depth-averaged (over near-bed control volume) bed-parallel velocity, with arrows showing velocity vectors as explained in text; (b) Bed-normal velocity at the top of the control volume; (c) Depth-averaged near-bed TKE; (d) Temporal rate of change of depth-averaged near-bed TKE; (e) Depth-averaged cross-shore advection of TKE along the bed; (f) Bed-normal advective fluxes at top of control volume. Plots (d)–(f) have the same color scale, positive (negative) values correspond to a gain (loss) in near-bed TKE. The black lines and circles depict the downward and upward zero-crossings of the water surface. Plot (g) shows the bed profile.

velocities are generally positive as waves propagate through the domain, except for the region with strong undertow velocities (around $x = 56.0$ m). Figure 10b shows the bed-normal velocity $\langle w_R \rangle$ at the top of the near-bed layer ($\zeta = D$). As addressed in section 3.2, $\langle w_R \rangle$ follows the orbital motion at locations before the bar crest ($x < 55.0$ m), leading to highest $\langle w_R \rangle$ under the wave front (offshore-to-onshore flow reversal). Between the crest and trough of the breaker bar ($x = 55.0$ to 58.0 m), $\langle w_R(D) \rangle$ is affected by the time-averaged clockwise circulation of fluid through the near-bed layer (section 3.2), which explains the predominantly negative (downward) $\langle w_R(D) \rangle$ around $x = 57.0$ m and positive (upward) around $x = 55.5$ m. For the following discussions, we emphasize that bed-normal and bed-parallel are directly related since $\langle w_R(D) \rangle \approx -{}^1/_D \mathrm{d}\langle \widehat{u}_R \rangle / \mathrm{d}x$. This also follows from Figure 10, where upward $\langle w_R(D) \rangle$ in plot (b) ("red regions") corresponds to converging $\langle \widehat{u}_R \rangle$ in plot (a), while downward $\langle w_R(D) \rangle$ ("blue regions") corresponds to diverging $\langle \widehat{u}_R \rangle$.

Figure 10c shows the spatiotemporal variation in depth-averaged TKE, $\langle \widehat{k} \rangle$, which was already discussed in section 4.2. Figure 10d shows the temporal rate of change of near-bed TKE, $\mathrm{d}\langle \widehat{k} \rangle / \mathrm{d}t$. At locations seaward of the bar crest ($x = 52$ – 54.5 m), positive $\mathrm{d}\langle \widehat{k} \rangle / \mathrm{d}t$ marks a gain in near-bed TKE that commences about halfway during the trough phase ($t/T \approx 0.8$) and lasts until the beginning of the wave crest phase ($t/T \approx 0.3$ to 0.5, depending on location). During the remainder of the crest phase and the early wave trough phase, near-bed TKE decreases ($\mathrm{d}\langle \widehat{k} \rangle / \mathrm{d}t < 0$). The TKE behavior is notably different along the steep slope between bar crest and trough ($x = 55.0$ to 58.0 m), where $\mathrm{d}\langle \widehat{k} \rangle / \mathrm{d}t$ is negative during most of the wave trough phase and increases sharply under the wave front (trough-to-crest transition). The time variation in the inner surf zone ($x > 58.5$ m) is relatively small.

These patterns in $\mathrm{d}\langle \widehat{k} \rangle / \mathrm{d}t$ can be partly explained by spatial gradients in horizontal and vertical transport of TKE. As detailed in section 2.5, TKE transport comprises a diffusive and an advective contribution, both of which can be split into bed-parallel and bed-normal components. All contributions were quantified (equations (7) and (8)). The advective fluxes typically exceed the diffusive fluxes by an order of magnitude. In addition, it was shown that the bed-normal influxes from the top ($\zeta = D$) were much greater than those from the bottom ($\zeta = z_b$). Hence, we restrict the analysis here to the two most significant transport terms: the TKE influx due to cross-shore advection $\widehat{\mathcal{A}}_x$ and the bed-normal influx from the outer flow to the near-bed layer $\mathcal{A}_z(D)$, respectively, shown in Figures 10e and 10f. Note that both influx terms are defined such that positive $\mathcal{A}$ corresponds to a gain in $\langle \widehat{k} \rangle$. Note that these terms do not fully explain the variation in $\mathrm{d}\langle \widehat{k} \rangle / \mathrm{d}t$: local production and dissipation (see section 4.5) are also significant but are not discussed again here for brevity.

In the shoaling region ($x = 52.0$ m) the cross-shore advective influx $\langle \widehat{\mathcal{A}}_x \rangle$ (Figure 10e) is dominated by orbital velocities. $\langle \widehat{\mathcal{A}}_x \rangle$ is positive under the propagating wave front, i.e., during the final stage of the trough half-cycle and the beginning of the crest half-cycle ($t/T = 0$ to 0.2). Conversely, $\langle \widehat{\mathcal{A}}_x \rangle$ is negative under the wave rear (around water surface zero down-crossing, $t/T = 0.3$ to 0.5), marking a net horizontal outflux of TKE. By comparing with Figures 10c and 10d, it becomes clear that this cross-shore advection yields a "concentration" of TKE under the wave front and a "dilution" under the wave rear—much like the changing field of suspended sand concentration under progressive surface waves, as described by, for example, Kranenburg et al. (2013). This process occurs irrespective of the wave breaking process further shoreward, and is instead directly related to the temporal behavior of $\mathrm{d}\langle \widehat{u}_R \rangle \langle \widehat{k} \rangle / \mathrm{d}x$ in the nonuniform flow field under progressive surface waves.

Further toward the bar crest, between $x = 53.0$ and 54.5 m, the temporal behavior of $\langle \widehat{\mathcal{A}}_x \rangle$ is similar to that at $x < 53.0$ m, but the magnitudes are higher. A region of positive bed-parallel influx commences at $x = 54.5$ m relatively early in the trough half-cycle ($t/T = 0.85$) and extends in the seaward direction during the remainder of the trough phase. This positive $\langle \widehat{\mathcal{A}}_x \rangle$ marks the arrival of seaward-advected TKE originating from the bar crest ($x \approx 55.0$ m). Conversely, a net cross-shore outflux of TKE ($\langle \widehat{\mathcal{A}}_x \rangle < 0$) is observed during the second half of the crest half-cycle, indicating that TKE is advected back in the shoreward direction. Hence, TKE travels back and forth between the bar crest and the shoaling locations, consistent with the observations of van der Zanden et al. (2016). Note that the intrawave cross-shore advection of TKE (Figure 10e) explains much of the time variation in TKE at $x = 53.0$ – 54.5 m seen in Figure 10d.

In the region between bar crest and trough ($x = 55.0$ to 57.0 m), where TKE is high, $\langle \widehat{\mathcal{A}}_x \rangle$ is dominated by time-averaged (undertow) velocities. Figure 10e reveals the presence of an almost continuous seaward-

directed transport cell, which drives a net flux of TKE from the toe of the breaker bar ($x = 56.0$ to 57.0 m; $\langle \widehat{\mathcal{A}}_x \rangle < 0$) toward the bar crest ($x = 55.0$ to 56.0 m; $\langle \widehat{\mathcal{A}}_x \rangle > 0$). This is explained because both undertow magnitudes and TKE increase from bar trough to bar crest in the seaward direction, due to (i) the influx of highly turbulent fluid from above (section 3.2) and (ii) the local near-bed production of TKE along the shoreward slope of the bar that exceeds dissipation (sections 4.4 and 4.5). This continuous transport cell is not fully interrupted by the passage of the wave crest ($t/T = 0.4$ to 0.7), but its location is shifted about 0.5 to 1 m shoreward.

Figure 10f shows the advective downward TKE influx by the bed-normal velocity $\langle w_R \rangle$. Note that $\langle w_R \rangle$ was previously explained in terms of orbital velocity motion and of two-dimensional time-averaged velocity circulations (see beginning of this section and Figure 10b). An almost continuous influx of TKE ($\langle \widehat{\mathcal{A}}_z \rangle > 0$) is observed at the lower section of the bar shoreward slope ($x = 56.0$ to 57.0 m) and at the bar trough ($x = 57.0$ to 58.0 m), while a continuous outflux occurs at the breaker crest ($\langle \widehat{\mathcal{A}}_z \rangle < 0$; $x = 55.0$ to 56.0 m). This influx and outflux can be interpreted as the bed-normal constituents of the advective transport cell through the near-bed layer that was identified in Figure 10e.

Comparison of Figures 10d and 10e–10f reveals that the time variation of TKE between the bar crest and trough is not simply the result of advected TKE that passes through the near-bed region. Instead, dk/dt is the result of a complex interplay between advection, production, and dissipation. This is most evident around the trough-to-crest flow reversal (around $t/T = 0.4$), when the bed-parallel influx of wave breaking turbulence (Figure 10e) does not only lead to a direct gain in near-bed TKE, but also enhances local turbulent production rates (Figure 8b), which together contribute to the sharp increase in TKE at the wave front (Figures 5b, 10c, and 10d).

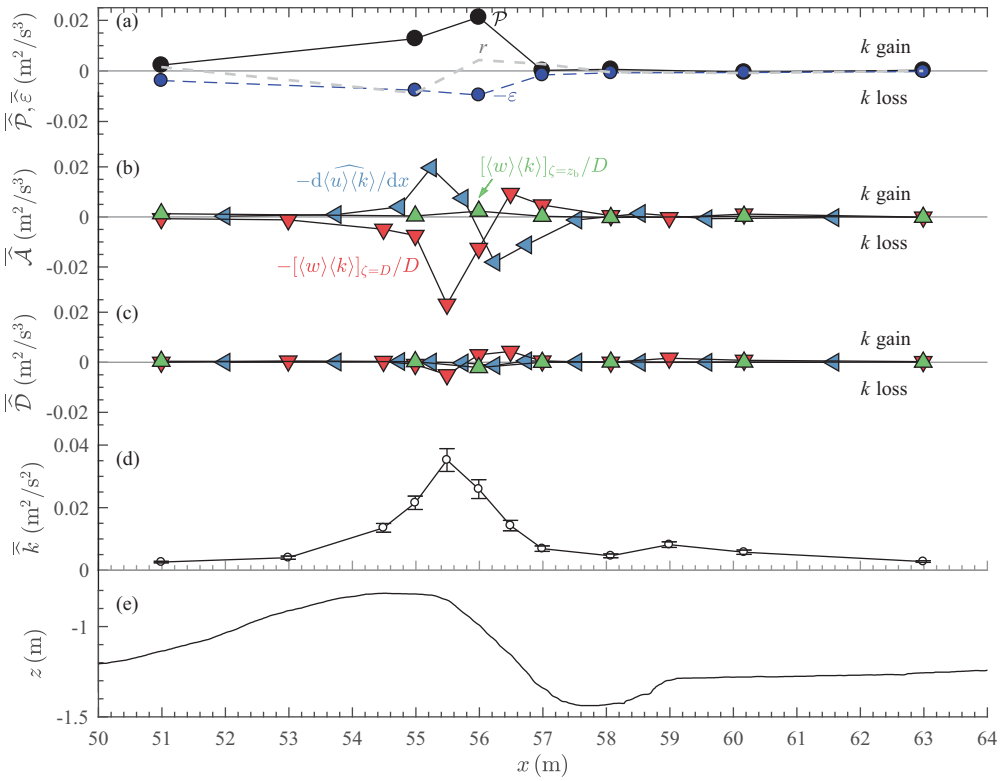

Figure 11. Time-averaged turbulent kinetic energy budget, depth-integrated over near-bed control volume ($\zeta = z_b$ to D). All terms are defined such that positive values correspond to an increase in near-bed TKE. (a) Contributions of production $\mathcal{P}$ (black circles and solid line) and dissipation ε (blue circles and dashed line), and residual term r (dashed grey line); (b) Advective contributions $\mathcal{A}$: cross-shore gradient of bed-parallel advection (blue $\triangleleft$), bed-normal-directed advective flux into control volume at $\zeta = D$ (red $\triangledown$), bed-normal-directed advective flux into control volume at $\zeta = z_b$ (green $\triangle$); (c) Diffusive contributions $\mathcal{D}$, with symbols as in plot (b); (d) Time-averaged TKE, depth-integrated over near-bed control volume, with error bars indicating 95% confidence interval; and (e) Bed profile.

4.7. Wave-Averaged TKE Budget

The previous sections addressed the local contributions of the major terms in the TKE budget. The present section discusses the wave-averaged TKE budget across the whole test section. The wave-averaged and depth-averaged TKE budget over the near-bed layer (equation (6)) can be written:

$$\overline{\widehat{\mathcal{P}}}-\overline{\widehat{\varepsilon}}+\overline{\widehat{\mathcal{A}}_x}+\overline{\mathcal{A}_z(D)}+\overline{\mathcal{A}_z(z_b)}+\overline{\widehat{\mathcal{D}}_x}+\overline{\mathcal{D}_z(z_b)}+\overline{\mathcal{D}_z(D)}+r=0\,, \tag{15}$$

where r denotes a residual term associated with pressure diffusion, which could not be quantified, and uncertainty errors in the computed terms and in the experimental setup (e.g., 3-D effects induced by the measurement frame and the flume side-walls). The residual term was quantified by evaluating equation (15) for all seven cross-shore locations. For this computation, and for the results that follow in this section, the time-averaged dissipation rate $\overline{\varepsilon}$ was calculated through equation (13) (Trowbridge & Elgar, 2001). The net advection of TKE ($\overline{\langle u\rangle\langle k\rangle}$, $\overline{\langle w\rangle\langle k\rangle}$) can be decomposed into current-related ($\overline{u}\,\overline{k}$, $\overline{w}\,\overline{k}$) and wave-related ($\overline{\langle\tilde{u}\rangle\langle\tilde{k}\rangle}$, $\overline{\langle\tilde{w}\rangle\langle\tilde{k}\rangle}$) contributions. This decomposition revealed that the net current-related and wave-related contributions are of similar magnitude in the shoaling region ($x \leq 52.0$ m), but in the breaking and inner surf zone, the current-related advection dominates ($> 90\%$) the total net advective transport. This relates to the strong undertow velocity and to the limited intrawave variation of $\langle k\rangle$ in this region, as also shown by van der A et al. (2017) in Figure 14).

Figure 11 shows all terms of equation (15), revealing that the main terms in the time-averaged TKE budget are production, dissipation, and the advective influxes in bed-parallel direction and in bed-normal direction at $\zeta = D$. The diffusive fluxes $\mathcal{D}$ and the upward advective influx of TKE from $\zeta < 0.001$ m, $\mathcal{A}_z(z_b)$, are both minor. The residual term r, which is of similar magnitude as the other terms, will be addressed in the discussion (section 5).

In the shoaling zone ($x \leq 52.0$ m) the net contributions from advection are limited. At these locations, near-bed TKE is predominantly controlled by local production and dissipation, which are approximately in equilibrium at a wave-averaged time-scale; this also holds for the inner surf zone ($x \geq 58.5$ m).

The area between the bar crest and the shoreward toe of the bar ($x = 54.0$ to 58.0 m) is the most interesting region in terms of TKE budget, with strong net advection in conjunction with production and dissipation rates that are not in local equilibrium. This region is also highlighted in Figure 12, which illustrates the two-dimensional advective circulation of TKE through the near-bed layer. Between the bar's shoreward slope

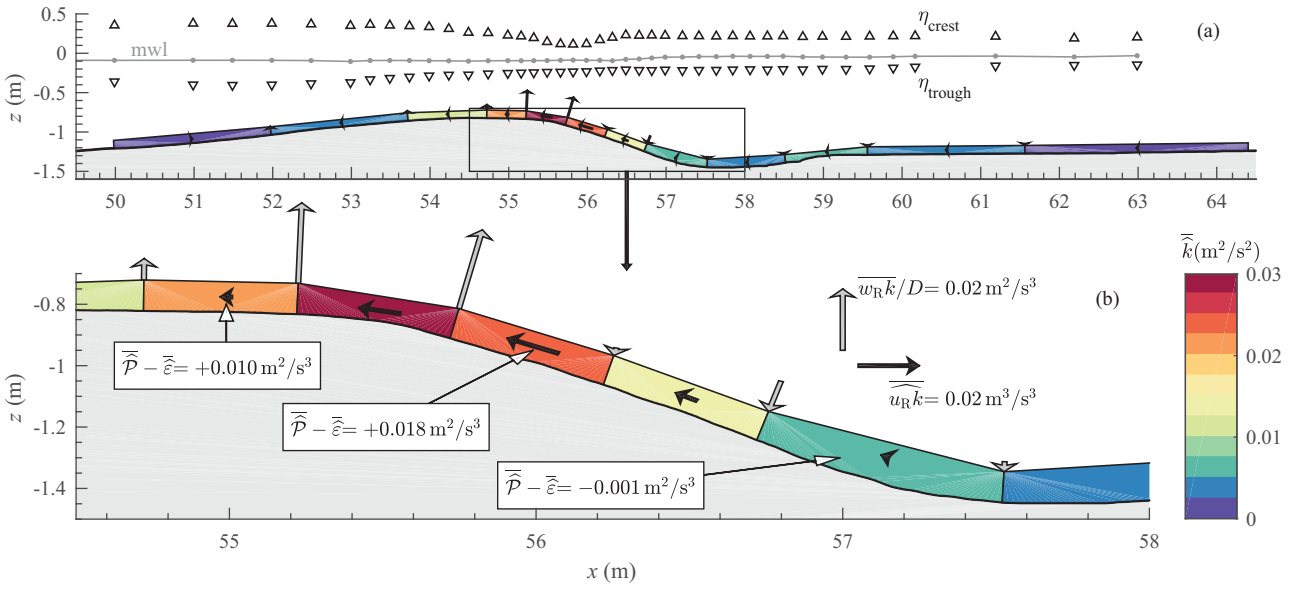

Figure 12. Illustration of time-averaged TKE transport through near-bed layer. Each colored rectangle depicts a near-bed control volume $\zeta = 0$ to 0.10 m, with color coding representing the time-averaged TKE level. Black arrows depict the direction and magnitude of the time-averaged bed-parallel advective plus diffusive transport of TKE, depth-averaged over the near-bed control volume. Grey arrows depict direction and magnitude of time-averaged bed-normal advective plus diffusive transport of TKE at top of control volume. For three locations, plot (b) shows the depth-averaged turbulence production minus dissipation rates.

and the bar trough ($x = 56.0$ to 58.0 m), the time-averaged undertow circulation and the large-scale periodic breaking vortex induce a downward influx of breaking-generated TKE into the near-bed layer (Figure 11b, red markers). This TKE is advected seaward along the bed, leading to net outflux ($\widehat{\mathcal{A}}_x < 0$) between $x = 56.0$ and 58.0 m and a net influx around the bar crest ($x = 54.0$ to 56.0 m; $\widehat{\mathcal{A}}_x > 0$). At these locations, the estimated turbulent production rate $\overline{\mathcal{P}}$ exceeds the dissipation $\overline{\varepsilon}$ by nearly a factor 2 (Figure 11a), leading to a further increase in $\overline{k}$. These high production rates are due to the presence of highly anisotropic breaking-generated turbulence in combination with strong flow nonuniformity that yields high velocity shear in the cross-shore and vertical directions (section 4.5). At the bar crest ($x = 54.0$ to 56.0 m), TKE is then advected upward from the near-bed region to the outer flow ($\mathcal{A}_z(D) < 0$). Note that the bed-normal TKE outflux at $x = 54.0$ to 56.0 m exceeds the bed-normal influx at $x = 56.0$ to 58.0 m (Figure 11b). Hence, the near-bed layer is a zone of net TKE production, rather than net dissipation, a finding that is discussed in detail in what follows (section 5).

5. Discussion

For the present measurements, the TKE balance could not be closed, leaving a residual term r with similar magnitude as the dominant physical terms (section 4.7). This is first attributed to the pressure diffusion term that could not be quantified using the present instrumental setup. Note that previous studies on wave breaking TKE (Chang & Liu, 1999; Clavero et al., 2016; Melville et al., 2002; Ting & Kirby, 1995) were also unable to resolve the pressure diffusion term and close the budget because of measurement limitations. Identical to the present study, the studies by Melville et al. (2002) and Clavero et al. (2016) found residual terms that were similar in magnitude to the advection, production, and dissipation terms. Note that Clavero et al. (2016), who measured the instantaneous flow field under small-scale breaking waves with high spatial coverage using particle image velocimetry, directly equated r to the pressure diffusion contribution. Such an approach does not seem justifiable for the present large-scale study: first, because of the coarser spatial resolution of the measurements, which introduces errors in the computed spatial gradients and hence in the advection and production estimates (as addressed in section 2.5); second, because of uncertainties in the dissipation rate estimation based on local point velocity measurements (as addressed in sections 2.5 and 4.5). Consequently, the residual term r in the TKE balance is likely due to the combination of pressure diffusion and measurement uncertainties.

The somewhat arbitrary choice for the near-bed layer ($\zeta = 0$ to 0.10 m) considered for the depth-averaged TKE budget analysis raises the question to what extent results would change had another layer thickness been chosen. The overall spatiotemporal behavior of all terms remains qualitatively similar. However, with a decreasing upper limit of the near-bed layer (i.e., the closer to the bed), local turbulence production, and dissipation become increasingly more significant relative to the horizontal and vertical advective transport terms.

A striking feature in the experiment is the high near-bed turbulent production, which exceeds the dissipation around the bar crest (sections 4.4 and 4.7). This result is somewhat surprising, as previous plunging wave experiments (Chang & Liu, 1999; Ting & Kirby, 1995) suggested that turbulence is predominantly produced at the water surface followed by net dissipation ($\varepsilon > \mathcal{P}$) in the water column. A fundamental difference between the present study and most previous experimental breaking wave studies is the scale. In the present study, the near-bed flow is in the rough turbulent flow regime around the bar crest whereas previous small-scale studies involved smooth beds and a transitional or even laminar WBL. Consequently, turbulence generation by bed shear stress is likely to be more significant in the present study, and the interaction between bed-shear-generated vortices and breaking vortices may contribute to the high production rates. A second significant difference is that the present study involves a barred profile, whereas most previous studies involved plane-sloping bed profiles. Note that the bar was "naturally" formed, by running the same regular breaking waves for about 100 min over an initially horizontal medium-sand test section, resulting in a bar that at both sides is steeper than those occurring on natural beaches (see discussion section in van der A et al., 2017). The bar will contribute to flow nonuniformity in the breaking region, for instance because the seaward-directed undertow converges between bar trough and bar crest, which will in turn favor turbulence production. This may also be another explanation for the relatively high "residual turbulence" in the present experiment, compared to previous nonbarred studies (see discussion in van der A et al., 2017).

An important result for numerical turbulence modeling is the incursion of wave breaking turbulence into the WBL, which significantly enhances TKE levels, even at elevations very close to the bed ($\zeta = 0.001$ m). This implies that near-bed TKE (k_b) under breaking waves cannot be accurately described by common empirical formulations of the form $k_b \sim u_*^2$ (e.g., Hinze, 1975), where u_* is the friction velocity calculated with friction factor based on nonbreaking wave observations. Instead, to improve the numerical modeling of near-bed TKE in surf zone conditions, it seems appropriate to consider alternative boundary conditions, e.g., a no-flux boundary condition ($dk/d\zeta = 0$) (as also advised by Hsu & Liu, 2004) or an adaptation of the friction factor to account for "external" turbulence effects on u_* (as measured by Fredsøe et al., 2003). Another important result is the significant contribution of turbulence production by normal stresses, which is explained by the anisotropy of the turbulent vortices. This turbulence production term cannot be accounted for in common turbulence closure models k–ε and k–ω, which often assume isotropic turbulence, although adapted models that consider turbulence anisotropy are available and have been applied to breaking waves (see e.g., Brown et al., 2016, for an overview).

The results of the present experiment can be compared with observations of sand transport processes during an accompanying mobile-bed experiment involving similar wave conditions and bed profile (van der Zanden et al., 2016, 2017a, 2017b). The overall distribution of near-bed TKE seen in the present study is qualitatively and quantitatively similar to observations from the mobile-bed experiment (van der Zanden et al., 2016). This relates to the dominant contribution of wave breaking turbulence to total TKE, which overpowers the differences in bed-shear-generated TKE due to different roughness and mobile versus fixed bed effects between both experiments. The time-averaged 2-D fluid circulation through the near-bed layer may largely explain the cross-shore distribution of suspended sand pick-up, advection and deposition reported in van der Zanden et al. (2017a). At the bar trough and lower section of the bar's shoreward slope, TKE is advected toward the bed and enhances local turbulent sand pick-up. The entrained sand is subsequently transported offshore toward the bar crest, where it is partly deposited as turbulence decays and is partly advected upward by the time-averaged velocity. Note that the upward-directed time-averaged velocity above the bar crest reaches values of up to 0.05 m/s (section 3.2), which is of similar magnitude to the settling velocity of medium sand (0.034 m/s for the accompanying mobile-bed experiment). Hence, these bed-normal velocities can contribute significantly to vertical advective mixing of suspended sediment. Indeed, the nearly depth-uniform vertical profiles of suspended sand above the bar crest indicate strong vertical mixing (van der Zanden et al., 2017a). Another important observation concerns the high near-bed Reynolds stresses in the wave breaking region (section 4.3). Assuming that these also induce high instantaneous bed shear stresses, one may expect significant effects on sand transport dynamics. Given that the instantaneous near-bed Reynolds stress is particularly high in the region between bar crest and bar trough, these stresses may partly explain the downslope, shoreward transport of sand as bedload observed by van der Zanden et al. (2017b).

6. Conclusions

Large-scale experiments involving a plunging wave over a barred bed profile with an immobile concrete top layer were conducted in a wave flume. LDA measurements of velocities were obtained within a 0.1 m thick near-bed layer at shoaling, wave breaking, and inner surf zone cross-shore locations. The measurements are used to explain the spatiotemporal variation in turbulent kinetic energy (TKE) near the bed in terms of local production and dissipation, and advective plus diffusive transport. The following is concluded from the results:

1. TKE inside the WBL, measured at 1 mm from the bed, increases by a factor 5 between the shoaling and breaking regions. This reaffirms previous, predominantly small-scale, laboratory experiments and indicates that near-bed TKE in the breaking region cannot be attributed solely to local bed shear.
2. Phase-averaged turbulent Reynolds stress at $z - z_{bed} > 0.02$ m in the breaking region has the same sign as the breaking-generated stress near the water surface. Close to the bed, at $z - z_{bed} = 1$ mm, the arrival of wave breaking turbulence and its interaction with bed-shear-generated turbulence leads to high magnitudes of the instantaneous Reynolds stress. However, the phase-averaged Reynolds stress between $z - z_{bed} = 0$ to 0.02 m shows similar phase behavior and has the same sign as the free-stream velocity, suggesting that the stress close to the bed is still largely controlled by bed-shear-generated turbulence.

3. Two-dimensional flow circulation is the main driver for the transport of breaking-generated TKE into and out of the near-bed layer on the shoreward slope of the bar. Incursion of TKE into the near-bed layer at the breaker bar trough occurs by means of advection rather than turbulent diffusion. TKE is then transported seaward to the breaker bar crest, where it leaves the near-bed layer through upward vertical advection.
4. Near-bed turbulence production is due to shear stresses and normal stresses. Production due to normal stresses results from the anisotropy of wave breaking turbulence in combination with the nonuniformity of the flow. In the shoaling and inner surf zones, local turbulence production and dissipation are roughly in equilibrium at a wave-averaged time scale. In the breaking region around the bar crest, production exceeds dissipation and the difference results in net advective transport of TKE.
5. The intrawave behavior of near-bed TKE is highly complex. In the shoaling zone, time-varying local production and dissipation explains the intrawave TKE behavior up to 0.02 m from the bed, approximately corresponding to the crest-phase WBL overshoot elevation. At higher elevations, the cross-shore advection of turbulence by orbital velocity contributes to "concentration" of TKE at the front of the progressing wave. At the bar crest, TKE is highest under the wave front, which is explained by a sudden increase in local production when the flow converges in the bed-parallel direction and accelerates in upward direction. At the shoreward slope between bar crest and trough, the time variation of near-bed TKE is largely explained by bed-parallel and bed-normal advection of turbulence.

Acknowledgments
The research presented in this paper was carried out within the SINBAD project, jointly funded by EPSRC (grants EP/J00507X/1 and EP/J005541/1) in the UK and by STW (grant 12058) in the Netherlands. The authors acknowledge the technical staff at the University of Aberdeen for help in preparing for the experiments and the CIEMLAB staff for assistance in conducting the experiments. The analysis presented benefited from the feedback from two anonymous reviewers and from helpful discussions with fellow SINBAD researchers. Data presented in this paper can be accessed through the 4TU data repository (https://doi.org/10.4121/uuid:753f1d84-36e5-47fa-b74b-55c288545b9b).

References

Akhavan, R., Kamm, R. D., & Shapiro, A. H. (1991). An investigation of transition to turbulence in bounded oscillatory Stokes flows: Part 1. Experiments. *Journal of Fluid Mechanics*, *225*(1), 395–422. https://doi.org/10.1017/s0022112091002100

Benedict, L. H., & Gould, R. D. (1996). Towards better uncertainty estimates for turbulence statistics. *Experiments in Fluids*, *22*(2), 129–136. https://doi.org/10.1007/s003480050030

Brown, S. A., Greaves, D. M., Magar, V., & Conley, D. C. (2016). Evaluation of turbulence closure models under spilling and plunging breakers in the surf zone. *Coastal Engineering*, *114*, 177–193. https://doi.org/10.1016/j.coastaleng.2016.04.002

Bryan, K. R., Black, K. P., & Gorman, R. M. (2003). Spectral estimates of dissipation rate within and near the surf zone. *Journal of Physical Oceanography*, *33*, 979–993.

Carstensen, S., Sumer, B. M., & Fredsøe, J. (2010). Coherent structures in wave boundary layers. Part 1. Oscillatory motion. *Journal of Fluid Mechanics*, *646*, 169–206. https://doi.org/10.1017/S0022112009992825

Carstensen, S., Sumer, B. M., & Fredsøe, J. (2012). A note on turbulent spots over a rough bed in wave boundary layers. *Physics of Fluids*, *24*(11), 115104. https://doi.org/10.1063/1.4767536

Chang, K. A., & Liu, P. L. F. (1999). Experimental investigation of turbulence generated by breaking waves in water of intermediate depth. *Physics of Fluids*, *11*(11), 3390–3400.

Chiapponi, L., Cobos, M., Losada, M. A., & Longo, S. (2017). Cross-shore variability and vorticity dynamics during wave breaking on a fixed bar. *Coastal Engineering*, *127*, 119–133. https://doi.org/10.1016/j.coastaleng.2017.06.011

Christensen, E. D. (2006). Large eddy simulation of spilling and plunging breakers. *Coastal Engineering*, *53*(5–6), 463–485. https://doi.org/10.1016/j.coastaleng.2005.11.001

Clavero, M., Longo, S., Chiapponi, L., & Losada, M. A. (2016). 3D flow measurements in regular breaking waves past a fixed submerged bar on an impermeable plane slope. *Journal of Fluid Mechanics*, *802*, 490–527. https://doi.org/10.1017/jfm.2016.483

Conley, D. C., & Inman, D. L. (1992). Field observations of the fluid-granular boundary-layer under near-breaking waves. *Journal of Geophysical Research*, *97*(C6), 9631–9643.

Costamagna, P., Vittori, G., & Blondeaux, P. (2003). Coherent structures in oscillatory boundary layers. *Journal of Fluid Mechanics*, *474*, 1–33. https://doi.org/10.1017/s0022112002002665

Cox, D. T., & Kobayashi, N. (2000). Identification of intense, intermittent coherent motions under shoaling and breaking waves. *Journal of Geophysical Research: Oceans*, *105*(C6), 14223–14236. https://doi.org/10.1029/2000JC900048

Deigaard, R., Fredsoe, J., & Mikkelsen, M. B. (1991). Measurements of the bed shear stress in a surf zone. In *Progress report/Institute of hydrodynamics and hydraulic engineering* (Vol. 73, pp. 21–30). Lungby, Denmark: Technical University of Denmark.

Dixen, M., Hatipoglu, F., Sumer, B. M., & Fredsøe, J. (2008). Wave boundary layer over a stone-covered bed. *Coastal Engineering*, *55*(1), 1–20. https://doi.org/10.1016/j.coastaleng.2007.06.005

Feddersen, F., Trowbridge, J. H., & Williams, A. J. (2007). Vertical structure of dissipation in the nearshore. *Journal of Physical Oceanography*, *37*(7), 1764–1777. https://doi.org/10.1175/jpo3098.1

Feddersen, F., & Williams, A. J. (2007). Direct estimation of the Reynolds stress vertical structure in the nearshore. *Journal of Atmospheric and Oceanic Technology*, *24*(1), 102–116. https://doi.org/10.1175/jtech1953.1

Fernandez-Mora, A., Ribberink, J. S., van der Zanden, J., van der Werf, J. J., & Jacobsen, N. G. (2016). RANS-VOF modeling of hydrodynamics and sand transport under full-scale non-breaking and breaking waves. In *Proceedings of the 35th Conference on Coastal Engineering* (15 pp.). Antalya, Turkey. https://doi.org/10.9753/icce.v35.sediment.29

Foster, D. L., Beach, R. A., & Holman, R. A. (2006). Turbulence observations of the nearshore wave bottom boundary layer. *Journal of Geophysical Research: Oceans*, *111*, C04011. https://doi.org/10.1029/2004jc002838

Fredsøe, J., Sumer, B. M., Kozakiewicz, A., Chua, L. H. C., & Deigaard, R. (2003). Effect of externally generated turbulence on wave boundary layer. *Coastal Engineering*, *49*(3), 155–183. https://doi.org/10.1016/S0378-3839(03)00032-2

George, R., Flick, R. E., & Guza, R. T. (1994). Observations of turbulence in the surf zone. *Journal of Geophysical Research: Oceans*, *99*(C1), 801–810. https://doi.org/10.1029/93jc02717

Hayashi, T., & Ohashi, M. (1982). A dynamical and visual study on the oscillatory turbulent boundary layer. In L. J. S. Bradbury et al. (Eds.), *Turbulent shear flows 3* (pp. 18–33). Berlin, Heidelberg: Springer.

Henriquez, M., Reniers, A. J. H. M., Ruessink, B. G., & Stive, M. J. F. (2014). PIV measurements of the bottom boundary layer under nonlinear surface waves. *Coastal Engineering*, *94*, 33–46. https://doi.org/10.1016/j.coastaleng.2014.08.004

Hino, M., Kashiwayanagi, M., Nakayama, A., & Hara, T. (1983). Experiments on the turbulence statistics and the structure of a reciprocating oscillatory flow. *Journal of Fluid Mechanics*, *131*, 363–400. https://doi.org/10.1017/S0022112083001378

Hinze, J. O. (1975). *Turbulence*. New York: McGraw-Hill.

Hsu, T. J., & Liu, P. L. F. (2004). Toward modeling turbulent suspension of sand in the nearshore. *Journal of Geophysical Research: Oceans*, *109*, C06018. https://doi.org/10.1029/2003jc002240

Hussain, A. K. M. F. (1986). Coherent structures and turbulence. *Journal of Fluid Mechanics*, *173*(1), 303. https://doi.org/10.1017/s0022112086001192

Jensen, B. L., Sumer, B. M., & Fredsoe, J. (1989). Turbulent oscillatory boundary-layers at high Reynolds-numbers. *Journal of Fluid Mechanics*, *206*, 265–297. https://doi.org/10.1017/S0022112089002302

Jonsson, I. G. (1980). A new approach to oscillatory rough turbulent boundary layers. *Ocean Engineering*, *7*(1), 109–152. https://doi.org/10.1016/0029-8018(80)90034-7

Justesen, P., Fredsøe, J., & Deigaard, R. (1987). *The bottleneck problem for turbulence in relation to suspended sediment in the surf zone*. Proceedings 20th International Conference on Coastal Engineering, Taipei, Taiwan.

Kemp, P. H., & Simons, R. R. (1982). The interaction between waves and a turbulent current: waves propagating with the current. *Journal of Fluid Mechanics*, *116*, 227–250. https://doi.org/10.1017/s0022112082000445

Kemp, P. H., & Simons, R. R. (1983). The interaction of waves and a turbulent current: waves propagating against the current. *Journal of Fluid Mechanics*, *130*, 73–89. https://doi.org/10.1017/s0022112083000981

Kimmoun, O., & Branger, H. (2007). A particle image velocimetry investigation on laboratory surf-zone breaking waves over a sloping beach. *Journal of Fluid Mechanics*, *588*, 353–397. https://doi.org/10.1017/s0022112007007641

Kranenburg, W. M., Ribberink, J. S., Schretlen, J. J. L. M., & Uittenbogaard, R. E. (2013). Sand transport beneath waves: The role of progressive wave streaming and other free surface effects. *Journal of Geophysical Research: Earth Surface*, *118*(1), 122–139. https://doi.org/10.1029/2012jf002427

LeClaire, P. D., & Ting, F. C. K. (2017). Measurements of suspended sediment transport and turbulent coherent structures induced by breaking waves using two-phase volumetric three-component velocimetry. *Coastal Engineering*, *121*, 56–76. https://doi.org/10.1016/j.coastaleng.2016.11.008

Lin, P. Z., & Liu, P. L. F. (1998). Turbulence transport, vorticity dynamics, and solute mixing under plunging breaking waves in surf zone. *Journal of Geophysical Research: Oceans*, *103*(C8), 15677–15694. https://doi.org/10.1029/98JC01360

Longo, S. (2009). Vorticity and intermittency within the pre-breaking region of spilling breakers. *Coastal Engineering*, *56*(3), 285–296. https://doi.org/10.1016/j.coastaleng.2008.09.003

Lumley, J. L., & Terray, E. A. (1983). Kinematics of turbulence convected by a random wave field. *Journal of Physical Oceanography*, *13*, 2000–2007.

Melville, W. K., Veron, F., & White, C. J. (2002). The velocity field under breaking waves: Coherent structures and turbulence. *Journal of Fluid Mechanics*, *454*, 203–233. https://doi.org/10.1017/s0022112001007078

Nadaoka, K., Hino, M., & Koyano, Y. (1989). Structure of the turbulent-flow field under breaking waves in the surf zone. *Journal of Fluid Mechanics*, *204*, 359–387.

Nadaoka, K., Ueno, S., & Igarashi, T. (1988). Sediment suspension due to large scale eddies in the surf zone. *Proceedings of the 21st International Conference on Coastal Engineering, Torremolimos, Spain* (pp. 1646–1660).

Nielsen, P. (1992). *Coastal bottom boundary layers and sediment transport* (Vol. 4). Singapore: World Scientific.

Pedocchi, F., Cantero, M. I., & García, M. H. (2011). Turbulent kinetic energy balance of an oscillatory boundary layer in the transition to the fully turbulent regime. *Journal of Turbulence*, *12*, N32. https://doi.org/10.1080/14685248.2011.587427

Peregrine, D. H. (1983). Breaking waves on beaches. *Annual Review of Fluid Mechanics*, *15*(1), 149–178. https://doi.org/10.1146/annurev.fl.15.010183.001053

Petti, M., & Longo, S. (2001). Turbulence experiments in the swash zone. *Coastal Engineering*, *43*(1), 1–24.

Pope, S. B. (2000). *Turbulent flows*. Cambridge, UK: Cambridge University Press.

Raubenheimer, B., Elgar, S., & Guza, R. T. (2004). Observations of swash zone velocities: A note on friction coefficients. *Journal of Geophysical Research*, *109*, C01027. https://doi.org/10.1029/2003jc001877

Ribberink, J. S., van der A, D. A., van der Zanden, J., O'Donoghue, T., Hurther, D., Cáceres, I., et al. (2014). *SandT-Pro: Sediment transport measurements under irregular and breaking waves*. Proceedings of the 34th International Conference on Coastal Engineering, Seoul, Korea. https://doi.org/10.9753/icce.v34.sediment.1

Sarpkaya, T. (1993). Coherent structures in oscillatory boundary layers. *Journal of Fluid Mechanics*, *253*(1), 105. https://doi.org/10.1017/s0022112093001739

Scandura, P. (2013). Two-dimensional vortex structures in the bottom boundary layer of progressive and solitary waves. *Journal of Fluid Mechanics*, *728*, 340–361. https://doi.org/10.1017/jfm.2013.274

Scandura, P., Faraci, C., & Foti, E. (2016). A numerical investigation of acceleration-skewed oscillatory flows. *Journal of Fluid Mechanics*, *808*, 576–613. https://doi.org/10.1017/jfm.2016.641

Scott, C. P., Cox, D. T., Maddux, T. B., & Long, J. W. (2005). Large-scale laboratory observations of turbulence on a fixed barred beach. *Measurement Science and Technology*, *16*(10), 1903–1912. https://doi.org/10.1088/0957-0233/19/10/004

Sleath, J. F. A. (1987). Turbulent oscillatory flow over rough beds. *Journal of Fluid Mechanics*, *182*(1), 369. https://doi.org/10.1017/s0022112087002374

Smith, E. R., & Kraus, N. C. (1991). Laboratory study of wave-breaking over bars and artificial reefs. *Journal of Waterway, Port, Coastal, and Ocean Engineering*, *117*(4), 307–325. https://doi.org/10.1061/(asce)0733-950x(1991)117:4(307)

Stansby, P. K., & Feng, T. (2005). Kinematics and depth-integrated terms in surf zone waves from laboratory measurement. *Journal of Fluid Mechanics*, *529*, 279–310. https://doi.org/10.1017/S0022112005003599

Sumer, B. M., Guner, H. A. A., Hansen, N. M., Fuhrman, D. R., & Fredsøe, J. (2013). Laboratory observations of flow and sediment transport induced by plunging regular waves. *Journal of Geophysical Research: Oceans*, *118*, 6161–6182. https://doi.org/10.1002/2013jc009324

Svendsen, I. A. (1987). Analysis of Surf Zone Turbulence. *Journal of Geophysical Research: Oceans*, *92*(C5), 5115–5124. https://doi.org/10.1029/JC092iC05p05115

Svendsen, I. A., Madsen, P. A., & Buhr Hansen, J. (1978). *Wave characteristics in the surf zone*. Proceedings of 16th Conference in Coastal Engineering, Hamburg, Germany.

Taylor, G. I. (1938). The spectrum of turbulence. *Proceedings of the Royal Society A: Mathematical, Physical and Engineering Sciences*, *164*(919), 476–490. https://doi.org/10.1098/rspa.1938.0032

Tennekes, H., & Lumley, J. L. (1972). *A first course in turbulence*. Cambridge, UK: Cambridge University Press.
Ting, F. C. K., & Kirby, J. T. (1995). Dynamics of surf-zone turbulence in a strong plunging breaker. *Coastal Engineering*, *24*(3–4), 177–204. https://doi.org/10.1016/0378-3839(94)00036-W
Trowbridge, J., & Elgar, S. (2001). Turbulence measurements in the surf zone. *Journal of Physical Oceanography*, *31*(8), 2403–2417.
van der A, D. A., O'Donoghue, T., Davies, A. G., & Ribberink, J. S. (2011). Experimental study of the turbulent boundary layer in acceleration-skewed oscillatory flow. *Journal of Fluid Mechanics*, *684*, 251–283. https://doi.org/10.1017/jfm.2011.300
van der A, D. A., van der Zanden, J., O'Donoghue, T., Hurther, D., Cáceres, I., McLelland, S. J., et al. (2017). Large-scale laboratory study of breaking wave hydrodynamics over a fixed bar. *Journal of Geophysical Research: Oceans*, *122*, 3287–3310. https://doi.org/10.1002/2016jc012072
van der Zanden, J., van der A, D. A., Hurther, D., Cáceres, I., O'Donoghue, T., & Ribberink, J. S. (2016). Near-bed hydrodynamics and turbulence below a large-scale plunging breaking wave over a mobile barred bed profile. *Journal of Geophysical Research: Oceans*, *121*, 6482–6506. https://doi.org/10.1002/2016jc011909
van der Zanden, J., van der A, D. A., Hurther, D., Cáceres, I., O'Donoghue, T., & Ribberink, J. S. (2017a). Suspended sediment transport around a large-scale laboratory breaker bar. *Coastal Engineering*, *125*, 51–69. https://doi.org/10.1016/j.coastaleng.2017.03.007
van der Zanden, J., van der A, D. A., Hurther, D., Cáceres, I., O'Donoghue, T., Hulscher, S. J. M. H., et al. (2017b). Bedload and suspended load contributions to breaker bar morphodynamics. *Coastal Engineering*, *129*, 74–92. https://doi.org/10.1016/j.coastaleng.2017.09.005
Veron, F., & Melville, W. K. (1999). Pulse-to-pulse coherent Doppler measurements of waves and turbulence. *Journal of Atmospheric and Oceanic Technology*, *16*, 1580–1597.
Vittori, G., & Verzicco, R. (1998). Direct simulation of transition in an oscillatory boundary layer. *Journal of Fluid Mechanics*, *371*, 207–232. https://doi.org/10.1017/s002211209800216x
Yoon, H. D., & Cox, D. T. (2010). Large-scale laboratory observations of wave breaking turbulence over an evolving beach. *Journal of Geophysical Research-Oceans*, *115*, https://doi.org/10.1029/2009jc005748
Yuan, J., & Dash, S. M. (2017). Experimental investigation of turbulent wave boundary layers under irregular coastal waves. *Coastal Engineering*, *128*, 22–36. https://doi.org/10.1016/j.coastaleng.2017.07.005
Zhou, Z., Hsu, T.-J., Cox, D., & Liu, X. (2017). Large-eddy simulation of wave-breaking induced turbulent coherent structures and suspended sediment transport on a barred beach. *Journal of Geophysical Research: Oceans*, *122*, 207–235. https://doi.org/10.1002/2016jc011884